Eur. Phys. J. D (2023) 77:19
https://doi.org/10.1140/epjd/s10053-023-00592-x

THE EUROPEAN PHYSICAL JOURNAL D

Theory and molecular simulations of plasma sputtering, transport and deposition processes

Pascal Brault[1,a], Anne-Lise Thomann[1], and Marjorie Cavarroc[2,b]

[1] GREMI CNRS – Université d'Orléans, 14 Rue d'Issoudun, BP6744, 45067 Orléans Cedex 2, France
[2] SAFRAN Tech, Rue des jeunes Bois, Chateaufort, CS 80112, 78772 Magny-Les-Hameaux, France

Received 3 November 2022 / Accepted 2 January 2023 / Published online: 01 February 2023
© The Author(s), under exclusive licence to EDP Sciences, SIF and Springer-Verlag GmbH Germany, part of Springer Nature 2023, corrected publication 2023

Abstract. The present review provides an overview of the basic theory of sputtering with recent models, focusing in particular on sputtered atom energy distribution functions. Molecular models such as Monte-Carlo, kinetic Monte-Carlo, and classical Molecular Dynamics simulations are presented due to their ability to describe the various processes involved in sputter deposition at the atomic and molecular scale as required. The sputter plasma, the sputtering mechanisms, the transport of sputtered material and its deposition leading to thin film growth can be addressed using these molecular simulations. In all cases, the underlying methodologies and some selected mechanisms are highlighted.

1 Introduction

Plasma sputtering is a widely used deposition method that belongs to physical vapor deposition (PVD) techniques. Its basic principle is the sputtering of a negatively biased target (called the cathode) by ions present in a (reactive) plasma. The plasma is ignited by the electrical breakdown when applying a high voltage between the cathode/target and the grounded part of the vessel or by an external antenna as in inductively coupled plasma (ICP) sources. In these cases ions are created in the plasma chamber. Those close to the target will be accelerated by the cathode potential fall. If they acquire enough energy, i.e., above a threshold (depending on the nature of the cathode/target), the impinging ions will sputter the target. The plasma source defines the operating regime: magnetron sputtering, cathodic sputtering using either a closed coupled plasma or an externally coupled plasma with a high frequency antenna. In all cases, the sputtering/deposition process comprises the following steps: ion creation, impingement of the ions on the biased target, sputtering of the target material and transport of the sputtered atoms toward the substrate.

During the flight to substrate, sputtered atoms can react with the plasma reactive species to form molecules, or if the pressure is high enough, atom condensation can occur, and cluster formation becomes possible in the plasma phase. The principle of plasma sputtering is summarized in Fig. 1.

There are several types of plasma sputtering. The most popular one is magnetron sputtering in which permanent magnetic fields are placed below the cathode so that the electrons are trapped, which has the effect of confining the ionization close to the cathode [2]. In turn, this increases the sputtering rate and the cathode current, while the positive ions created impinge the target with an energy corresponding to the cathode negative bias V_{b}, with the maximum value of eV_{b}. Variants using different types of magnet result in different sizes of plasma in front of the substrate, as summarized in Fig. 2.

The cathode can be powered by continuous or pulsed direct current (DC), alternative current (AC), or radiofrequency (RF) sources. An improvement is to use a pulsed DC source with a high-power very short pulse duration, the so-called HiPIMS (high-power impulse magnetron sputtering) or HPPMS (high-power pulsed magnetron sputtering) [3]. For all these configurations, the sputtering gas can be either neutral (e.g., argon, helium) or reactive (e.g., oxygen, nitrogen, ammonia, methane, often mixed with a non-reactive gas such as argon, helium, etc.) [4]. DC sputtering requires that the target remain conductive during the entire process.

Studying the sputtering process requires finding what is common to all these configurations. However, it is also important to focus on different specific issues in order to understand how plasma features are affected. The basic information sought is the nature of the sputtered species, the sputtering yields, i.e., the ratio of sputtered atoms per incident ions, and the energy distribution

[a] e-mail: pascal.brault@univ-orleans.fr (corresponding author)
[b] e-mail: marjorie.cavarroc@safrangroup.com

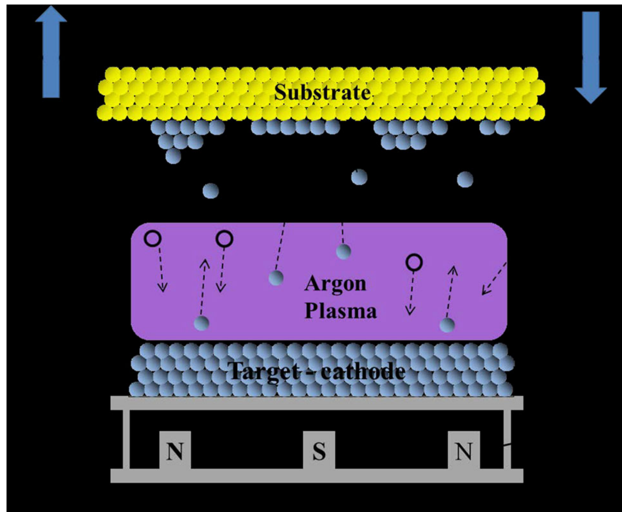

Fig. 1 A simple schematic of plasma sputtering. Reprinted from Ref. [1]

functions. The present study will describe how analytical modeling and computer simulations deal with calculating and/or predicting these parameters, but will also describe the generated plasma itself.

The general scheme of simulations, highlighting the necessary steps to be accomplished to fully describe magnetron plasma sputter deposition, called "virtual sputter magnetron" [5] is summarized in Fig. 3.

This review will be organized along the three main components, plasma and sputtering -transport-deposition/growth, for plasmas with a bias below 1 kV. Ion sputtering/implantation in the keV region and above are beyond the scope of this review. While Sect. 2 is devoted to sputtering theory, the third section presents Monte-Carlo approaches to magnetron discharge modeling. The fourth section is devoted to the different numerical simulations of plasma sputtering, transport and deposition using atomistic models: Monte-Carlo, kinetic Monte-Carlo, and Molecular Dynamics.

2 Sputtering models

This part reviews the basic concepts of sputtering from the point of view of target sputtering as well as the properties of the sputtered material.

The theory of sputtering aims at describing the physics of the interaction of an incoming ion with atoms of a material. Depending on the colliding atom or the ion kinetic energy, successive phenomena occur at the surface and in the depth of the target, which results in the ejection of an atom as described in Fig. 4 [6].

Sputtering theory provides an analytical formula to obtain the sputtering rate γ_{sputt}, i.e. the ratio of the number of sputtered target atoms N_{t} to the number

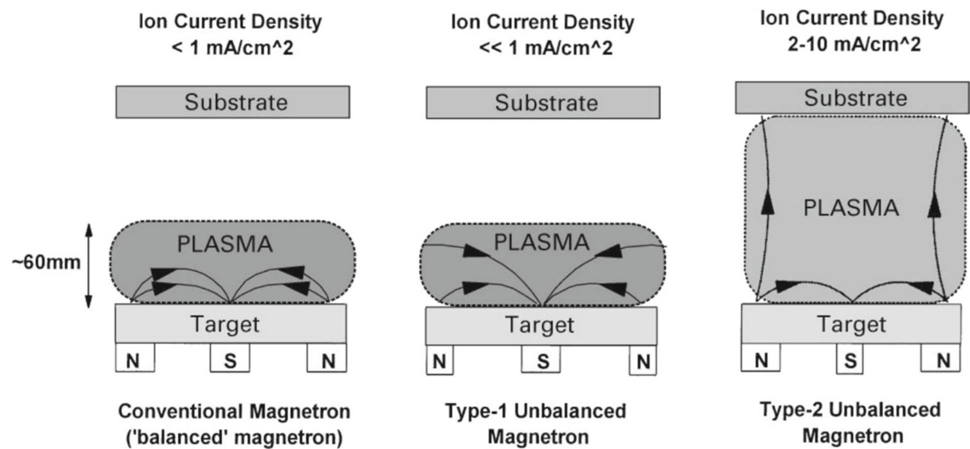

Fig. 2 Different types of magnetron configurations. Reprinted from Ref. [2]

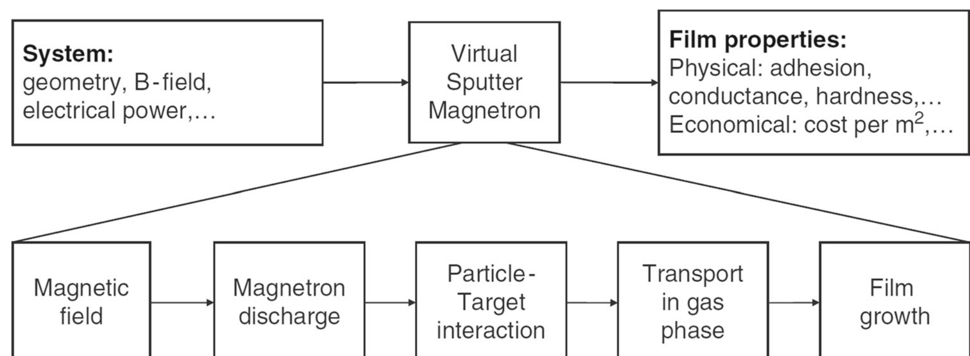

Fig. 3 General scheme of the simulation parts needed to build a "virtual sputter magnetron". Reprinted from Ref. [5]

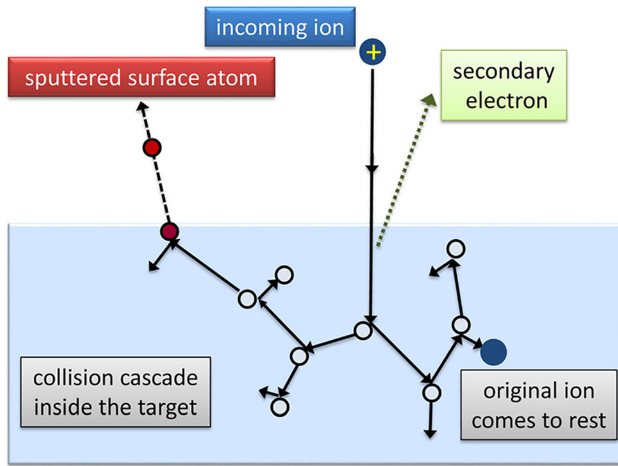

Fig. 4 Schematic describing the main steps of a sputtering event resulting from the interaction of an incoming ion with target atoms up to surface atom ejection and the original ion coming to rest in the target (Reprinted from Ref. [6])

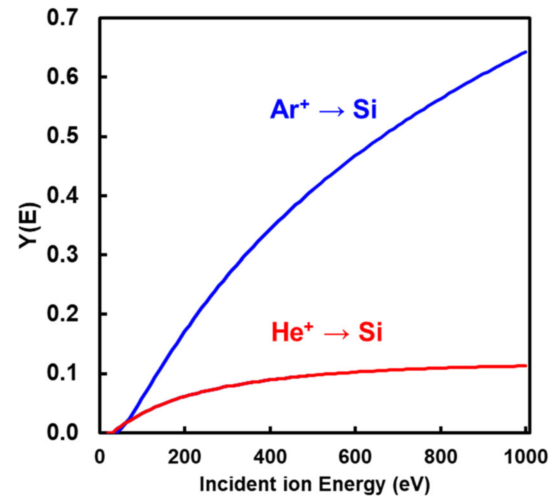

Fig. 5 Plot of the sputtering yields of Si by Ar^+ and He^+ ions with kinetic energies up to 1000 eV calculated from Eq. (1)

of incident ions N_i, i.e. $Y = \frac{N_t}{N_i}$, and the energy distribution function of the sputtered atoms. For complex systems such as molecular solids (metal oxides, organics, etc.), more than one species or molecules and small clusters can be ejected, making it almost impossible to deduce a practical analytical formula. In these cases, it will be more appropriate to use atomistic modeling (see Sect. 5 below).

Many publications have addressed the foundation of sputtering mechanism theories [2, 4–43]. The pioneering theory proposed by Townes in 1944 [7] provided the first analytical expression of sputtering yield in a glow discharge, depending on cathode fall and discharge current, since the initial experimental work reported in 1852 [44] by Grove. Reasonable agreement with experiment was found at low bias voltage and high pressure. The next most referenced contribution came from Sigmund's work [15, 16, 22, 24, 32] dedicated to both sputtering yields and the kinetic energy distribution of sputtered species of pure and multicomponent targets.

A frequently used analytical sputtering yield γ_{sputt}[45, 46] is provided in the form:

$$Y(E) = 0.042\frac{Q(Z_2)\alpha^*(m_g/m_s)}{U_s}\frac{S_n(E)}{1+\Gamma k\varepsilon^{0.3}}\left[1-\sqrt{\frac{Eth}{E}}\right]^s \quad (1)$$

where E is the incoming sputtering ion energy, m_g and m_s are the masses of ion and target atom in atomic mass units respectively, and the numerical factor in units of Å^{-2}. U_s is the target surface binding energy, Eth is the sputtering threshold energy, $S_n(E)$ is the stopping power, and Γ, Q and α^* are (fitting) parameters [45]. It is based on the Sigmund theory [15] using the Ziegler–Biersack–Littmark (ZBL) [47] screened repulsive potential and including the Lindhard electronic stopping power [48]. As sputtering can only occur if the surface is able to break its bond with neighboring surface atoms, the incoming ions should exceed a threshold energy Eth. This energy threshold is a function of the surface atom binding energy E_s [45]:

$$E_{\text{th}} = E_s\begin{cases} 1+1.57\dfrac{m_i}{\gamma.m_t}; & m_i < m_t \\ \dfrac{6.7}{\gamma}; & m_i \geq m_t \end{cases} \quad (2)$$

and with $\gamma = 4\frac{m_i m_t}{(m_i+m_t)^2}$ being the energy transfer in a direct collision. All the parameters needed for evaluating $Y(E)$ are available in Refs. [6, 45].

On the other hand, the sputtering yield scales with ion energy as [5].

$$Y(E) = aE^b \quad (3)$$

a and b being adjustable parameters that depend on the nature of the incoming ion (for kinetic energy less than 3 keV) and the target material [6]. Fitted values of a and b are available in Ref. [6].

For illustration, Fig. 5 displays the sputtering yields of silicon by Ar^+ and He^+ ions in the range 0–1000 eV, calculated from Eq. (1). The effect of the mass ratio γ is clearly visible: a large difference in the masses of impinging ions and a defined target element results in a lower sputtering yield.

A second important parameter is the sputtered atom energy distribution function, since it describes the energy that will be deposited during deposition after traveling the path from target to substrate. During flight, the sputtered atoms will lose energy by collision with the background plasma-forming gas. This will impact the energy distribution function at the substrate.

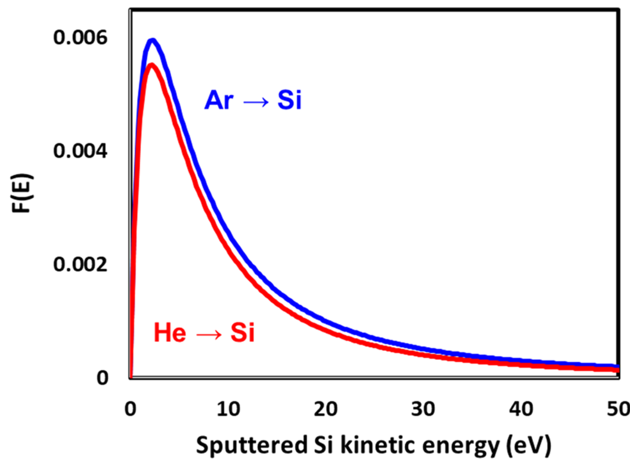

Fig. 6 The Thompson Energy Distribution function (Eq. 4) of sputtered Si by Ar and He ions calculated at the same kinetic energy of 400 eV

A very popular sputtered atom energy distribution function (EDF) F(E) was developed by Thompson [19], which reads:

$$F(E)\begin{cases}\propto \frac{1-\left(\frac{E_s+E}{\gamma E_i}\right)^{\frac{1}{2}}}{E^2\left(1+\frac{E_s}{E}\right)^3}, & E<\gamma E_i - E_s\\ =0, & E>\gamma E_i - E_s\end{cases} \quad (4)$$

where E_s is the binding energy of the target surface atoms, and E is the energy of the sputtered atoms.

This EDF behaves as E^{-2} for a large sputtered atom energy E, showing that the contribution of the distribution tail can be significant. The maximum of the distribution is located at $E_s/2$ and the width is on the order of a few eV (5 to 20 eV) when the incoming ion is Ar. Figure 6 displays the example of Si sputtered by Ar and He. Contrary to the sputtering yield, the different mass ratios do not significantly affect the sputtered atom EDF.

An analytical improvement in the sputtered atom EDF was recently achieved and is known as the Stepanova EDF [39, 40], which reads:

$$F(E)=\frac{E}{(E+E_s)^3}\exp\left[-A\left(\frac{m_i(E\cos^{q_1}\theta+E_s)}{m_t E_i}\right)^{q_2}\right] \times\left(1-\frac{E+E_s}{E_{\max}+E_s}\right) \quad (5)$$

where $E_{\max}$ is a cutoff factor allowing $F(E)$ to vanish for $E>E_{\max}$ with $E_{\max}=\frac{E_s}{E_{\text{th}}}E_i$, $q_1\approx 2-\frac{m_t}{4m_i}$, $q_2 = 0.55$ and $A=13$ [39].

It accounts for anisotropy effects at low incident ion energy which results in narrowing of the EDF in agreement with Monte-Carlo simulations [49, 50]. This effect is not included in the Thompson distribution. To illustrate how Stepanova EDF behaves, Fig. 7 displays a typical comparison with experiments, modeling, and Thompson distribution.

Other deviations from the Thompson formula have been observed in the case of light incident ions impacting heavy target atoms. Assuming that sputtered atoms are only primary recoil atoms, the following Falcone formula was derived [32]

$$F(E)=\frac{E}{(E+E_s)^{5/2}}\ln\frac{\gamma E_i}{E+E_s} \quad (6)$$

A further slight improvement, also for light ion sputtering, was carried out by Kenmotsu [46, 51], leading to:

$$F(E)=\frac{E}{(E+E_s)^{8/5}}\left[\ln\frac{\gamma(1-\gamma)E_i}{E+E_s}\right]^2 \quad (7)$$

Note that contrary to the Thompson formula (4), the Falcone and Kenmotsu EDF formulae depend on the incoming energy E_i. Moreover, anisotropic effects at low energy are not considered, as in Thompson distribution.

Figure 8 displays a comparison between EDFs described by the various EDF formulae for light and heavier ions at 2 different energies. Since the Kenmotsu formula is optimized for light ions, it fails to produce a reasonable EDF for Ar^+ ion sputtering at low energy, as shown in Fig. 8a. The incident energy dependence of the Stepanova, Kenmotsu and to a lesser extent Falcone formulae is well observed. For Falcone the dependence is more visible for light ion He^+, since the Falcone formula holds for light ions.

After the sputtering occurs, the sputtered materials as well as the reflected incident ions travel across the plasma which is mainly composed of neutral species since the ionized species fraction in DC, RF or pulsed DC magnetron sputtering ranges from 10^{-5} to 10^{-3}. This can reach a value close to 1 in an HiPIMS configuration. Sputtered atoms traveling across the region between target and substrate, will suffer collisions with the ambient gas and lose part of their kinetic energy modifying their EDF. An elegant analytical approach has been developed which considers, in a first approximation, the energy losses along a pathway normal to the substrate, i.e., without accounting for angular effects [52, 53]. The mean kinetic energy is thus, at distance d from the target, is thus given by:

$$E_F=(E-k_BT_g)\left[\frac{E_f}{E_i}\right]^n+k_BT_g \quad (8)$$

E_F being the kinetic energy after n collisions. $\frac{E_f}{E_i}=1-\gamma/2$ is the kinetic energy ratio after and before a collision. $n=\mathrm{d}P\tau/k_\mathrm{B}T_\mathrm{g}$ is the number of collisions along the path, P and T_g are the sputtering gas pressure and temperature, and τ is the collision cross section assuming, for example, hard core interactions. The energy loss (E_f) of the sputtered atoms with the gas atoms is calculated considering a Maxwell–Boltzmann (MB) distribution at $E_g=k_BT_g$. For each E_g in the MB gas

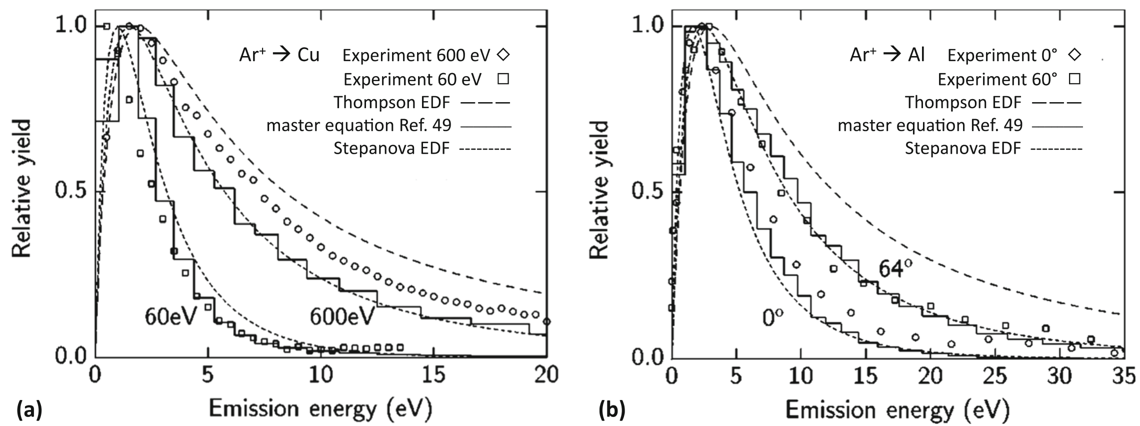

Fig. 7 Plots of the Stepanova energy distribution function compared to the Thompson distribution, master equation (stepped lines) and experiments at different ion incident energies for Ar^+ on Cu (**a**) and angles for Ar^+ on Al (**b**). Adapted from Figs. 10, 11 of Ref. [39]

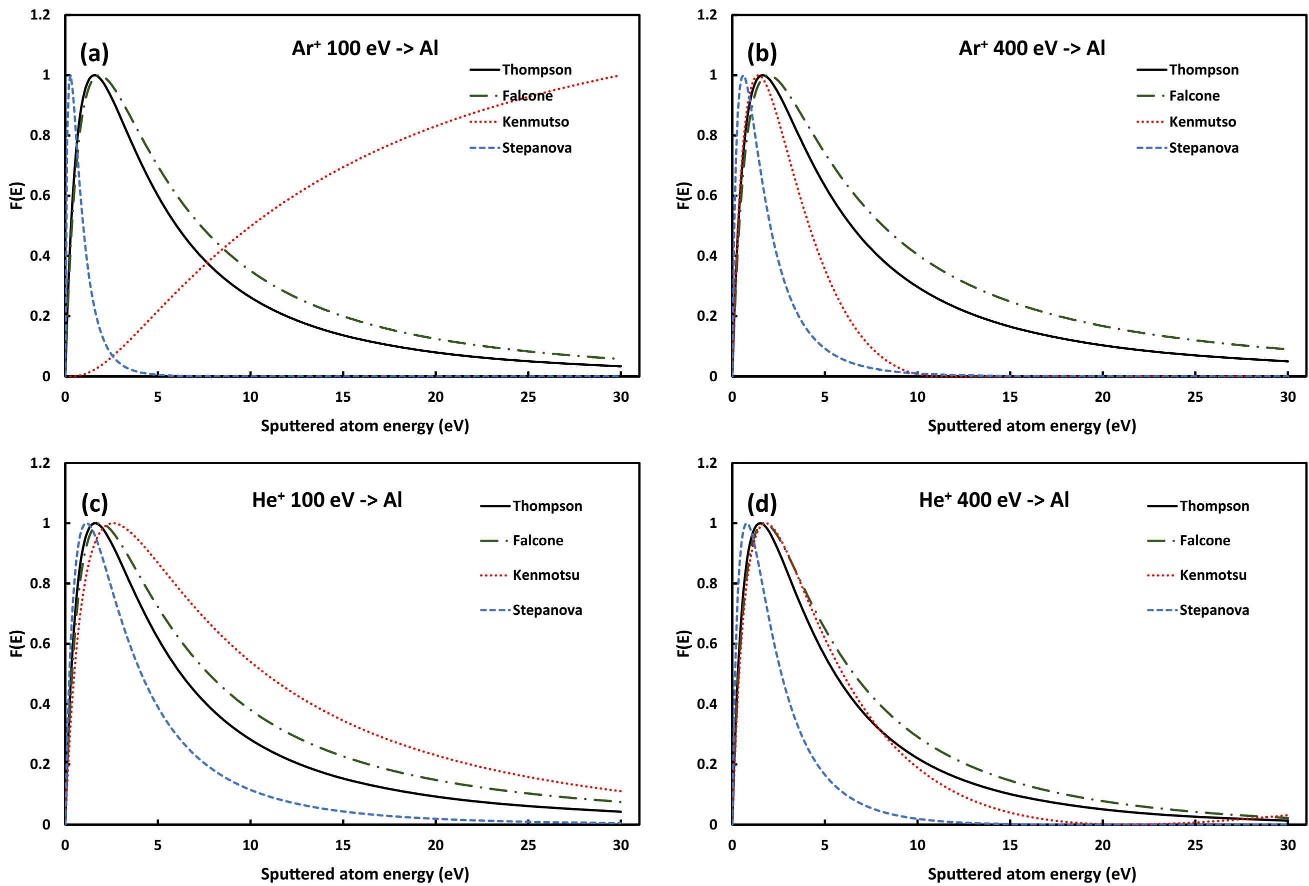

Fig. 8 Plots of Thompson, Falcone, Kenmotsu and Stepanova Energy distribution functions for (**a**, **b**) incident Ar^+ and **c**, **d** incident He^+ ions, both with kinetic energy of 100 and 400 eV

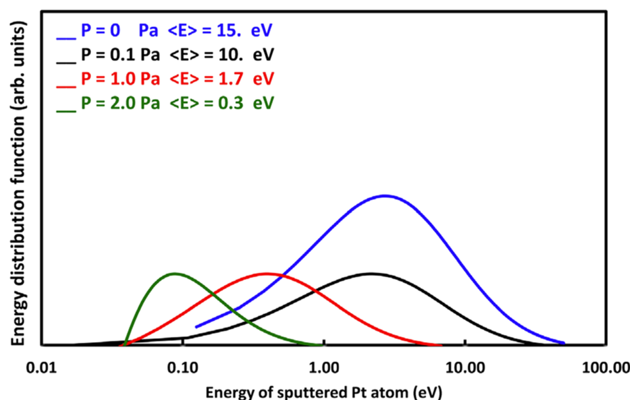

Fig. 9 Example of sputtered Pt atom EDF for a fixed target to substrate distance $d = 10$ cm and varying pressure. The target potential is fixed at 300 V. For clarity, a log scale is used for the horizontal energy scale. Mean kinetic energies of the resulting EDFs are reported for each pressure. Reprinted from Ref. [54]

distribution, the energy loss is calculated for a fixed value of the kinetic energy E of a sputtered atom. This is repeated for each E of any EDF $F(E)$, and weighted by the collision probability, which is simply the convolution of $F(E)$ and the MB distribution at T_g [52]. It should be mentioned that the key parameter in Eq. (5) is the product $P.d$ that drives the collision number n: varying P or d keeping $P.d$ constant thus resulting in the same $f(E)$ at distance d from the target. Figure 9 shows how the EDF evolves against pressure P. At sufficiently high P or d values, the sputtered atom EDF becomes a Maxwell–Boltzmann distribution.

For the specific case of HiPIMS, this procedure can be used provided that the EDF accounting for both neutral and ions is properly included.

Reactive magnetron sputtering is a more complex situation since the ambient (sputtering) gas, often a mixture of a reactive gas such as O_2, NH_3, CH_4, etc., can react with the target subjected to the incident ions. In unreactive sputtering by inert gases, it is expected that ions implanted in the target will not modify the sputtering, mainly because these ions do not react and do not modify the properties of the physical target, except for local distortions of the lattice. Even if this assumption is questionable, it underlies almost all sputtering models. When reactive species interact with the target, both chemical composition and physical properties (conducting/semi-conducting and insulating state) are changed. Change in the target chemical composition due to reactive species is often called the target poisoning effect. Moreover, it depends on which reactive flux, the (initially conducting) target is exposed to. And thus, the sputtering can be severely affected A simple analytical model known as Berg's model [55–63] has been devised and provides sputtering rates (as well as deposition rates). It is based on the balance between the removal of the poisoned part and interaction with the non-poisoned part of the targets. It also assumes a reactive diatomic molecule gas mixed with the sputtering inert gas (Ar, for example) and that the molecules formed are diatomic with one metal atom and one reactive atom (for example, AlO with O_2 gas). Extension to more complicated reactive molecules and a metal target is possible but more complicated to address [63]. A detailed description is provided in Ref. [63]. Basically, at steady state, a fraction θ_t of the target area A_t is poisoned by the reactive gas, while 1-θ_t remains unaffected. It is thus assumed that removal of a compound is balanced by the formation of a target compound. On the other hand, part of the unreacted metal can be sputtered by the sputtering gas.

So the total sputtering yield $Y = Y_c + Y_m$ with

$$Y_c = \frac{q}{JA_t}\alpha 2F\frac{1-\theta_t}{\theta_t} \tag{9}$$

Y_m is the yield of unreacted sputtered atoms given by the analytical formula (8) or available in the literature. 2F is the flux of reactive atoms (resulting from the dissociation of the corresponding reactive diatomic molecule) with $F = \frac{P}{\sqrt{2\pi m k_B T}}$ and P is the reactive gas partial pressure, m the mass of the reactive molecule, T the gas temperature, k_B the Boltzmann constant. J is the ion current density ($J.m^{-2}$) at the magnetron target. Formula (8) assumes that the compound coverage is known.

More complex situations such as multimetallic targets and multi reactive gases have been addressed, providing relatively simple formulae that can help to rapidly predict erosion rates and also deposition rates. Nevertheless, it should be borne in mind that these formulae result from crude approximations that do not take into account the many-body nature of the interaction with and inside the target.

3 Magnetron discharge modeling using Monte-Carlo simulations

Many reviews and book chapters have addressed (reactive) magnetron plasma modeling [4, 64–69] and articles have focused on specific issues, such as ion and neutral transport, erosion profiles of the target, reactive transport, magnetic field, ionization, etc. [70–112].

In Monte-Carlo (MC) simulations, computational test particles that represent a large number of real plasma particles are followed. They move due to the applied forces and collisions are included using probabilities and random numbers. This technique is very easy to implement and fast to compute. Its main disadvantage is that the forces must be an input, i.e., the simulation is not self-consistent. Many processes have been described using this technique: understanding of the transport and collision properties of the charged particles in magnetron discharges, effect of the magnetic field, ionization map in 2D simulations, ion motion, erosion profile of the target and its effect on magnetic

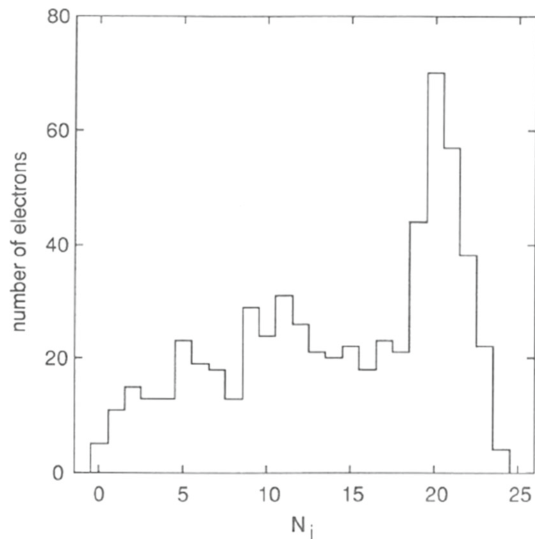

Fig. 10 Distribution of number of ionizing collisions N_{i} for 600 electrons in argon at a pressure of 1 Pa. This histogram has a peak centered at 20 ionizations, which corresponds to electrons that lose all their energy in collisions without escaping from the magnetic trap. Elastic, excitation, and ionizing collisions are taken into account. The maximum possible number of ionizations is $N_{\max} = 25$, which is the ratio of the 400 V cathode potential to the 15.8 V ionization potential. The width of the peak is due to energy lost in excitation collisions. Reprinted from Ref. [113]

field distribution [113–128]. The method can be implemented in 3D and can address magnetron sputtering reactors [129–134].

The plasma species obey the equations of motion in an ExB field [113, 123]:

$$m\frac{d\vec{v}}{dt} = q\left(\vec{E} + \vec{v} \times \vec{B}\right) + \vec{F}_{coll} \tag{10}$$

$$\frac{d\vec{x}}{dt} = \vec{v} \tag{11}$$

with $\vec{x}, \vec{v}$ the position and velocity, respectively, $\vec{E}, \vec{B}$ the electric and magnetic field, and $\vec{F}_{coll}$ the collisional force accounting for momentum change. The collision term is calculated using the MC method. In a first attempt, elastic, excitation, and ionization collisions can be included. Elastic collisions lead to momentum change, while excitation and ionization collisions lead to energy losses. At each time step, it is determined whether a collision (between the electron and a nearby atom of the background gas) could occur. This is done by generating a random number, which is compared to the collision probability. Depending on the type of collision, the energy of the colliding electron is lowered to a specified amount. It can be reasonably approximated that the energy lost in an excitation or ionizing collision can be a fixed amount, 11.6 eV for excitation and 15.8 eV for ionization of argon. This defines the energy threshold at which the electron is effective. For ionization events, the kinetic energy of the emitted secondary electron is ignored, since this energy is almost always much smaller than the energy of the ionizing electron [135]. In addition to reducing the energy of the energetic electron when it undergoes a collision, its velocity is randomly chosen consistently with the corresponding differential scattering cross section. For energies $E_e < 3$ eV, differential cross sections are assumed to be isotropic. For 3 eV $< E_e <$ 3 keV, tables of normalized values of $d\sigma/d\Omega$ for elastic scattering [136] can be chosen. Figure 10 shows the distribution of ionizing electron collisions with Argon at $P = 1$ Pa, $V_{\mathrm{b}} = -400$ V [113].

The location of ionization is used to define the target racetrack, i.e. the zone where the ions normally sputter the target. In fact, Fig. 11 shows the link between the etch profile of the racetrack and the ionization density above the target. It is important, therefore, to calculate this plasma parameter in order to determine and predict the target erosion.

A very powerful technique is PIC-MCC [137], which includes the calculation of the electric field produced by the external power source and the spatial distribution of the plasma charged particles in an MC simulation. The whole simulation thus becomes self-consistent. Since this topic deserves a review article in itself, the reader is advised to read the fully detailed reviews by Bogaerts' group [5, 67, 138] and the extensions to HiPIMS processes [105, 109]

MC simulations are also carried out to calculate the transport of sputtered materials from the target to the substrate as well as the growth of the resulting

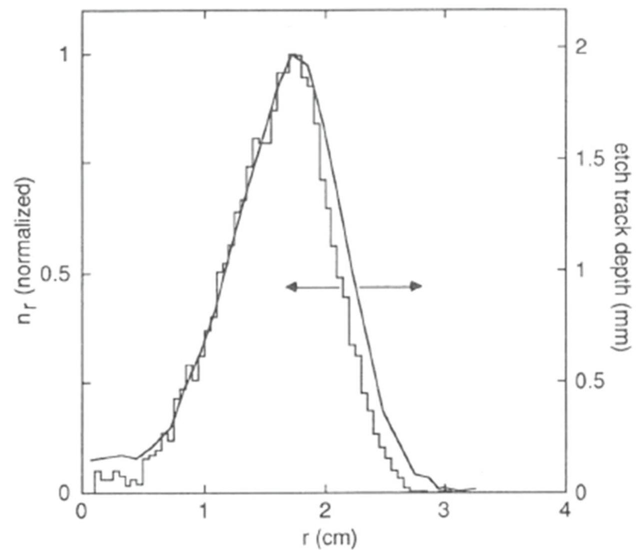

Fig. 11 Radial profile of ionizing collisions, $n_{\mathrm{r}}(r)$, from the simulation, compared to etch track depth from experimental measurements. The vertical scales for the two curves were adjusted to make the heights of their peaks match. The agreement is good. Reprinted from Ref. [113]

films. This is addressed in the next section, which also includes Molecular Dynamics simulations.

4 Molecular Models of sputtering, transport and deposition

Since the processes of sputtering, (collisional) transport, deposition and growth are driven by atomic, molecular interactions, atomistic approaches are expected to be relevant.

4.1 Monte-Carlo models

As stated above for electron motion in the discharge, collisions as well as neutrals can be handled statistically using Monte-Carlo models. The Monte-Carlo method [139–141] has also been successfully applied to sputtering [142–158] and sputtered material transport [70, 159–174]. Kinetic Monte-Carlo simulations are able to address deposition and the resulting thin film growth [175–194].

The most popular Monte-Carlo code of ion sputtering is the SRIM-TRIM [142] extended to multicomponent targets such as TRYDIN [143].

The impact of an incoming ion is treated using a binary collision approximation (BCA), which means that there are no many-body contributions and each collision includes only two colliding partners [145] without the memory of the past event: each collision is statically independent of the previous one. Each trajectory starts with a given position, direction, and energy of the ion. The ion is then followed through a sequence of collisions with target atoms, assuming a straight free travel path between collisions. Each collision lowers the particle energy by the amount of electronic energy loss and by the so-called nuclear energy loss, i.e. the energy transferred to the target atom in the collision. The target atom receiving an amount of energy which exceeds a preset value (e.g. the surface binding energy E_{S}), is called a primary knock-on atom (PKA). Its motion and subsequent collisions will be followed in the same way as those of the incident ion. The same occurs with any higher generation of recoil atoms (SKA = secondary knock-on atoms), which are created after further collisions. The motion of an incident ion or recoil atoms is terminated either when the energy drops below a prescribed value (usually chosen as E_{S}), or when the particle has moved out of the front or rear surface of the target. The target is considered amorphous with atoms at random locations, which means that any directional effects such as channeling are not considered here.

In three-dimensional space, initial conditions of the incoming ion are defined by velocity (kinetic energy) and angle of incidence and azimuthal angle, as displayed in Fig. 12, for example.

The collided partner will move upon collision, and angles and velocities are selected in the appropriate distribution after selecting some random numbers. These quantities are calculated using the impact parameter P which defines the closest approach distance between the two collision partners via the relation:

$$1-\frac{V(r_0)}{E_i}-\left(\frac{P}{r_0}\right)^2=0 \tag{12}$$

where r_0 is the closest approach distance, P is the impact parameter, E_{i} is the kinetic energy of the incoming collider. $V(r)$ is an interaction potential between the incoming ion and the target atom, chosen to be a repulsive screened Coulomb potential, such as ZBL, Molière, etc.

To define the output of the collision, the relevant parameters, impact parameter and angles, are randomly selected. The impact parameter is defined as $P_{\max}=\pi^{-1/2}\ \mathrm{N}^{-1/3}$, where N is the atomic density of the target material. A uniform random number R_P $(0<R_p<1)$ is selected such that the randomly selected impact parameter $=P_{max}\sqrt{R_p}$. The center of mass deviation angle θ is defined as, $\cos\theta=\frac{P+\rho+\delta}{\rho+r_0}$, δ being a small additional term [145]. The laboratory deviation ψ angle is defined as $\psi=arctan\left(\frac{\sin\theta}{\cos\theta+m_i/m_t}\right)$.

Finally, the azimuthal angle is randomly chosen as $\varphi=2\pi R_a$ $(0<R_a<1)$. The energy E_f after the collision (in the center of mass) in a binary collision (Fig. 12) is:

$$E_f=E_i\frac{4m_im_t}{(m_i+m_t)^2}\sin^2\left(\frac{\theta}{2}\right)$$

The electronic energy loss is approximated by different functions depending on the energy range considered [143]. At the low ion energy of interest in magnetron sputtering, the electronic energy loss ΔE_e is written:

$\Delta E_e=kE_i^p$ with $p=\frac{1}{2}$ and k the Lindhard-Scharff [48] formula:

$$k=k_l=\frac{1.212Z_i^{\frac{7}{6}}Z_t}{\left(Z_i^{\frac{2}{3}}+Z_t^{\frac{2}{3}}\right)^{\frac{3}{2}}m_i^{\frac{1}{2}}}$$

In this way all the relevant parameters of the sputtered materials can be calculated: Velocity distribution functions, angle distributions, as well as implanted and backscattered ion parameters.

The main limitations are the amorphous nature of material and the binary collision approximation. Moreover, the calculation of the sputtering yields does not take into account the history of the target, i.e., it is carried out with a virgin amorphous material and thus does not account for preferential sputtering (this is done by the TRYDIN-TRIM version [146]) nor for the effects of voids, implanted ions and any outermost surface, such as roughness.

Another popular code is the ACAT code [151–157] from Yamamura. It is based on a different way of calculating the successive collision events and makes use

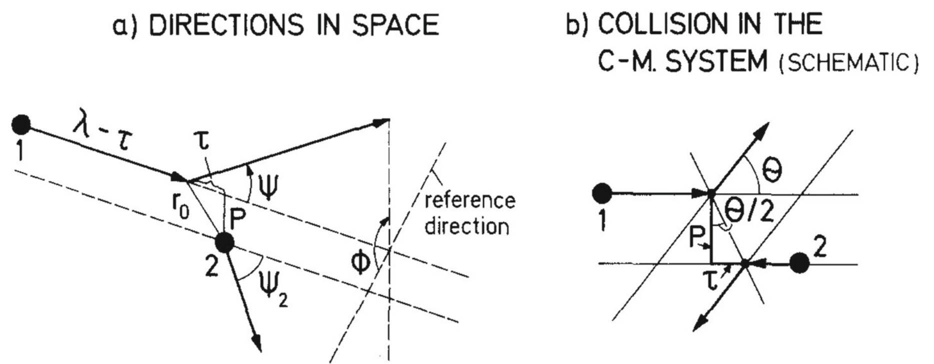

Fig. 12 **a** Directions of flight of projectile (ion or recoil) and of knock-on in 3-dimensional space. **b** Collision in the center-of-mass system (schematically drawn for a hard-sphere-collision). Reprinted from Ref. [142]

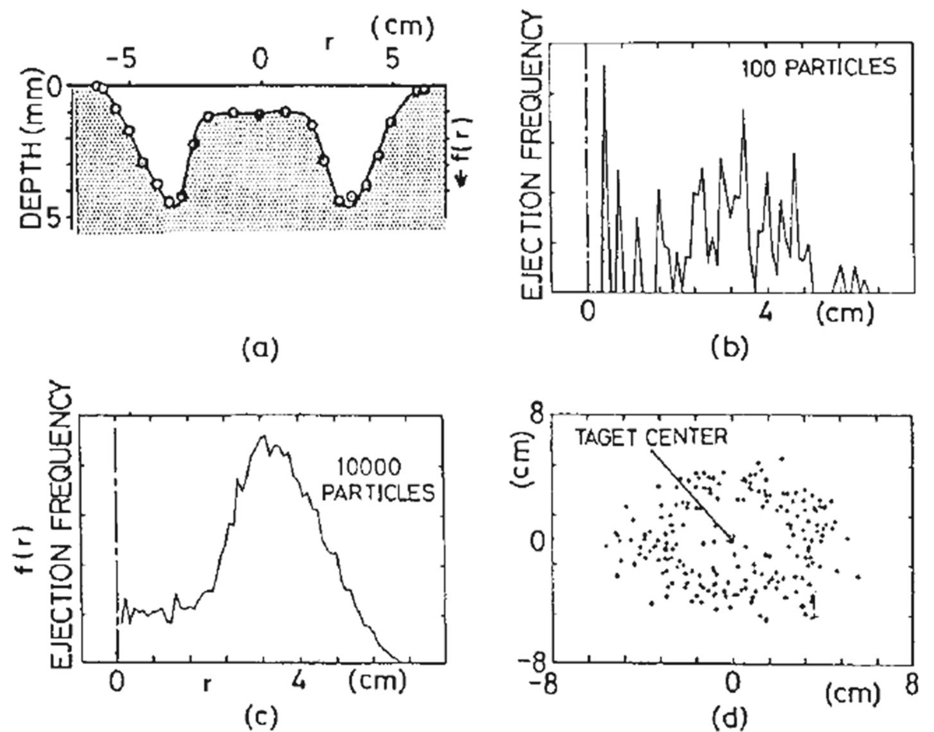

Fig. 13 **a** Experimental radial erosion profile. **b** and **c** Distributions of computer-generated radial ejection positions of the first 100 and 10 000 particles using the experimental profile (**a**). **d** Two-dimensional computer-generated ejection points of the first 200 particles on the target. Reprinted from Ref. [158]

of the repulsive Molière potential for ion target interactions. Nevertheless, it is its fitted analytic formula that is widely used for the sputtering yield dependence on ion energy [155].

The TRIM and ACAT strategies aim at calculating the history of the incoming ions in order to determine sputtering features. Another way, which is more statistical, involves considering the statistics of the ejected species based on the experimental erosion profile of the target [158]. To define the initial position of the sputtered atoms, a radial distribution function of the ejection point F(r) is connected with the experimental erosion profile function f(r) (Fig. 13a) as: $F(r)$ dr = $f(r)2\pi$r dr

We thus calculate the quantity:

$$a_m = \frac{\sum_{n=1}^{m} F(dr.n)}{\sum_{n=1}^{N} F(dr \cdot n)} \tag{13}$$

with dr being the radial spacing between points and N the total number of radial intervals. Then we search for a uniform random number $\varepsilon_1 \in [0,1]$ which is compared to a_{m}: $\varepsilon_1 \leq a_m$. Thus, from the minimal value of m satisfying this relation, the sputtered atom initial radial position $r = \mathrm{dr}.m{-}\mathrm{d}r/2$ can be determined.

Figure 13b and c displays the radial distribution of sputtering position. We have a 2D coordinate system by including the azimuthal angle ϕ through a new uniform random number $\varepsilon_2 \in [0,1[$ and $\phi = 2\pi\varepsilon_2$, which gives the coordinates (r, ϕ). Figure 13d provides the 2D positions of 200 positions on the target.

At this position (r, ϕ), it remains to find the ejection angles. This is achieved by considering an ejection angle distribution for the direction normal to the surface and the azimuthal angles θ and φ, respectively. Uniform random numbers ε_3 and $\varepsilon_4 \in [0,1[$are selected. When θ obeys a cosine law, i.e. $\frac{P(\theta)d\theta}{2\pi \sin \theta d\theta} = C.\cos^{\gamma}\theta$, then

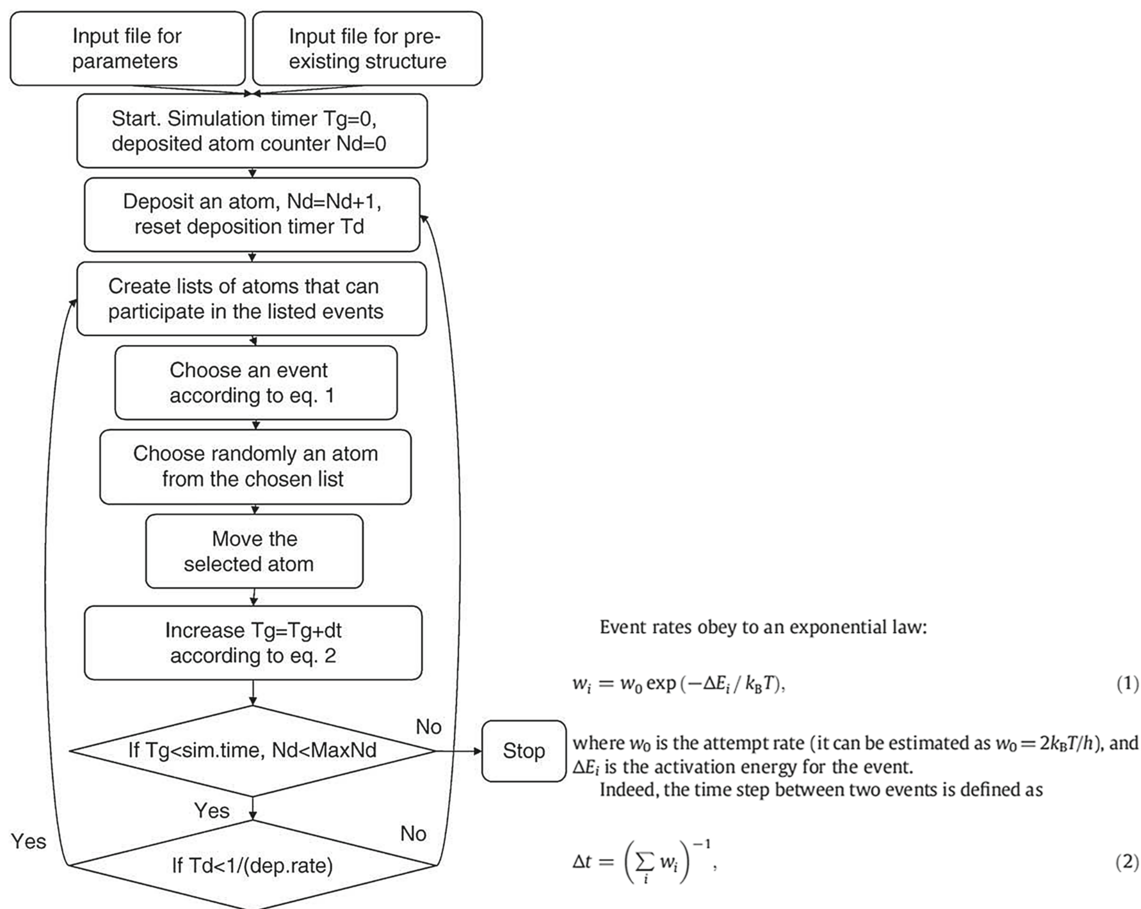

Fig. 14 (Left) Flowchart of the NASCAM model; (Right) Eq. 1 and 2 from Ref. [177]. In this case, the time interval is not sampled from a Poisson distribution. Reprinted from Ref. [177]

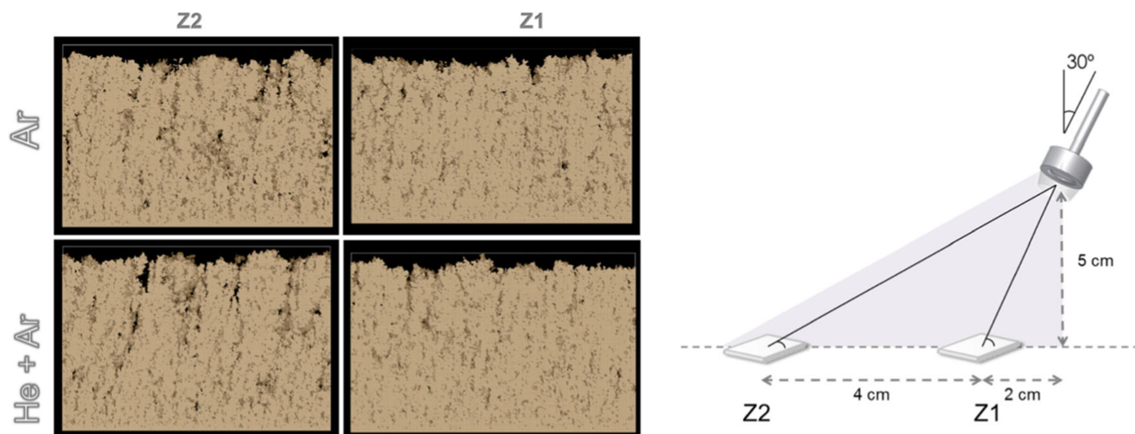

Fig. 15 (left) kMC simulations of the growth at different deposition angles with different plasma compositions Ar and He + Ar. (right) positions Z1 and Z2 of the corresponding experimental setup defining the deposition angle. Reprinted from Ref. [189]

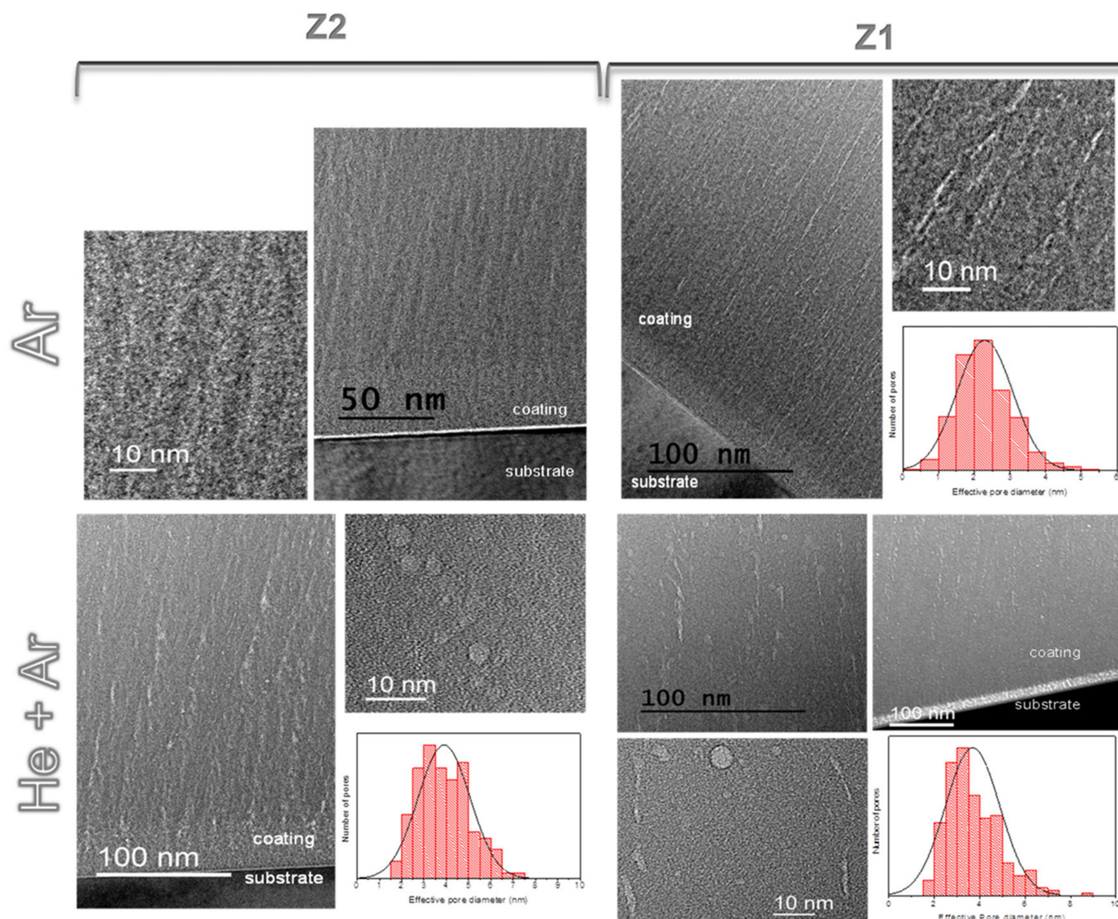

Fig. 16 The transmission electron microscopy pictures corresponding to kMC on Fig. 15, with porosity size distribution Reprinted from Ref. [189]

$\theta = \cos^{-1}\left\{\varepsilon_3^{1/\gamma+1}\right\}$. The azimuthal angle is selected by $\varphi = 2\pi\varepsilon_4$.

It should be pointed out that this technique is dependent on the local surface geometry of the target and thus is extended to consider rough surfaces [88, 90].

4.1.1 Transport of sputtered species.

When sputtered atoms are emitted, they have to travel the target to substrate distance d, and depending on the pressure P, they have some probability to collide with plasma/gas species. The mean free path λ gives the distance between 2 collisions and is expressed as [161]:

$$\lambda^{-1} = 4\sqrt{2}\pi\frac{P_T}{kT}r_t^2 + \pi\frac{P_g}{kT}(r_t + r_g)^2\left(1 + \frac{m_t}{m_g}\right)^{1/2} \tag{14}$$

with P_{T} and P_{g} the partial pressure of the sputtered target and gas atoms, respectively.

m_{T} and m_{g} are the corresponding masses, r_{T} and r_{g} the corresponding atomic radii.

Since $P_{\mathrm{T}} << P_{\mathrm{g}}$, the first term in Eq. (18) vanishes. Moreover, the mean free path is energy dependent: an empirical fit suggests that λ should be multiplied by a factor E^{a}, with $a = 0$ when $E < 1$ eV and $a = 0.29$ when $E > 1$ eV, leading to:

$$\lambda = E^a / \left(\pi\frac{P_g}{kT}(r_t + r_g)^2\left(1 + \frac{m_t}{m_g}\right)^{1/2}\right)$$

Between two collisions, the travel distance λ^* of sputtered atoms is randomly chosen using a Poisson distribution: $\lambda^* = \lambda \ln\left[1/(1\text{-}\varepsilon_5)\right]$, with ε_5 a uniform random number in [0, 1[. The next step is to determine the scattering angle θ_{com} and the energy loss of the sputtered atom. In the center of mass frame, and for a spherical atom–atom pair interaction, the scattering angle θ_{com} reads:

$$2\theta_{\mathrm{com}} = \pi - 2b\int_{r_0}^{\infty}\frac{dr}{r^2\{1 - [V(r)/E_{\mathrm{com}}] - (b^2/r^2)\}^{1/2}} \tag{15}$$

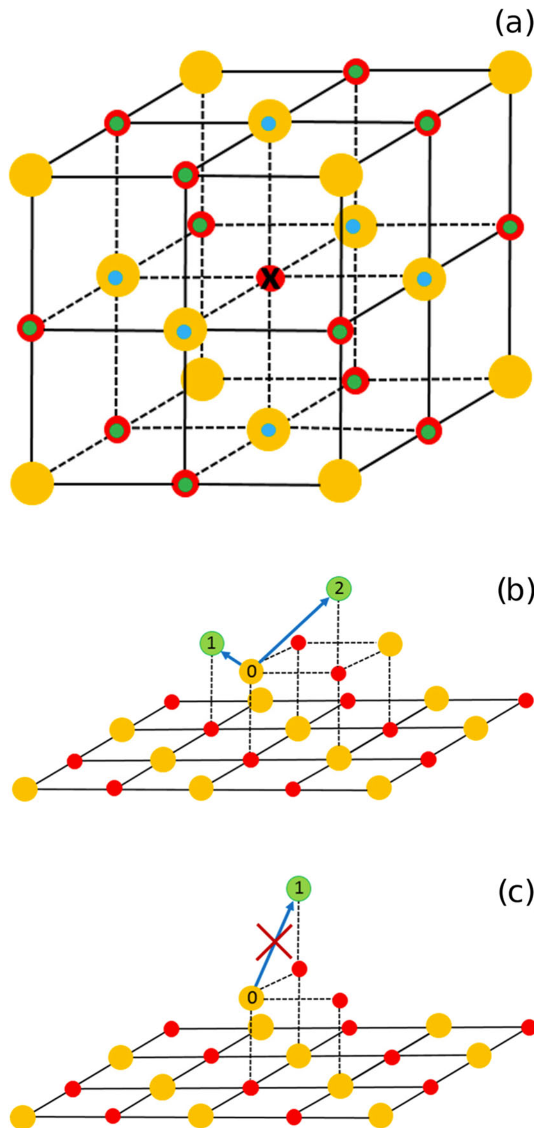

Fig. 17 **a** Representation of the NaCl-type lattice cell of TiN: Ti atoms (large yellow spheres) and N atoms (small red spheres) occupy their own fcc sublattice positions. Two possible final sites (**b**) and a forbidden final site (**c**) for a diffusing Ti atom. Reprinted from Ref. [192]

and r_0 is defined as $b^2 = r_0^2\left(1 - \frac{V(r_0)}{E_{\text{com}}}\right)$ (similar to Eq. 21). B is the impact parameter lying between 0 and $b_{\max}$. $b_{\max}$ defines the smallest deviation angle, which is arbitrarily defined, for example corresponding to $\theta_{\text{com}} \leq 0.286°$ [161]. b is selected as $b = b_{\max}\varepsilon_5$, with ε_5 a uniform random number in [0, 1].

V(r) is the interaction potential between the sputtered atoms and the gas atoms. It is often chosen as a repulsive form such as Molière, Kr–C, ZBL, etc., interaction potentials [47] of the form

$$V(r) = \frac{Z_t Z_g e^2}{r} g(r)$$

where $g(r)$ is a screening function.

The polar scattering angle θ_{lab} in the laboratory frame is calculated as:

$$\theta_{\text{lab}} = \tan^{-1}\left(\frac{\sin\theta_{\text{com}}}{\cos\theta_{\text{com}} + m_T/m_g}\right)$$

while the azimuthal angle φ_{lab} is randomly selected between 0 and 2π. After collision with a gas atom, the sputtered atom energy loss is written:

$$E_{\text{newlab}} = E_{\text{lab}}\left(1 - \frac{2(1-\cos\theta_{\text{com}})m_g m_T}{(m_g+m_T)^2}\right)$$

The energy loss is calculated until the sputtered particle reaches the substrate. Moreover, the kinetic energy of the sputtered particle is compared to a prescribed mean kinetic energy corresponding to the gas temperature. When it occurs, the sputtered particle is considered as thermalized and continues with this energy until it reaches the substrate. This procedure should be built while preserving a Maxwell–Boltzmann energy distribution at the gas temperature T_{g}. One way to achieve this is by randomly selecting the corresponding energy. Another way is to convolute the calculated energy distribution with the Maxwell–Boltzmann gas energy distribution [52, 53].

Since the sputtered atoms approach the substrate with a defined energy distribution function, a growth model can be designed.

4.1.2 Kinetic Monte-Carlo growth models.

Kinetic Monte-Carlo growth models aim at simulating growth phenomena from a prescribed list N of possible events with an occurrence probability based on known rate constants k_{i}, $i = 1, \ldots, N$. Moreover, this method is able to calculate the time interval of the event realization by selecting a uniform random number $\varepsilon \in]0, 1]$, such that $\Delta t = -\frac{\ln\varepsilon}{\sum_i k_i e^{\frac{-E_i}{kT}}}$, E_{i} being the barrier height of the process i. This enables various processes, with different time scales, to be calculated simultaneously. Thus, long time diffusion becomes accessible. Reachable time lengths such as a few ms have been reported. In fact, there is no time limit since it depends only on reaction rate magnitudes.

Many data are required in order to build a kMC model. All possible or selected events should be recorded in a first step. For example, the growth may originate from a vapor of n different species with fraction α_{i}, a flux F_{i} toward the substrate surface and a sticking probability s_{i} and E_{ik} barrier to process k. The method requires that the placement of the atom be predefined on a 3D grid that defines the expected crystalline positions. The crystal structure of the deposit or the surface does not necessarily have to be prescribed. The deposition of amorphous films can be achieved by randomly deforming the bond lengths and angles of a predefined structure [187].

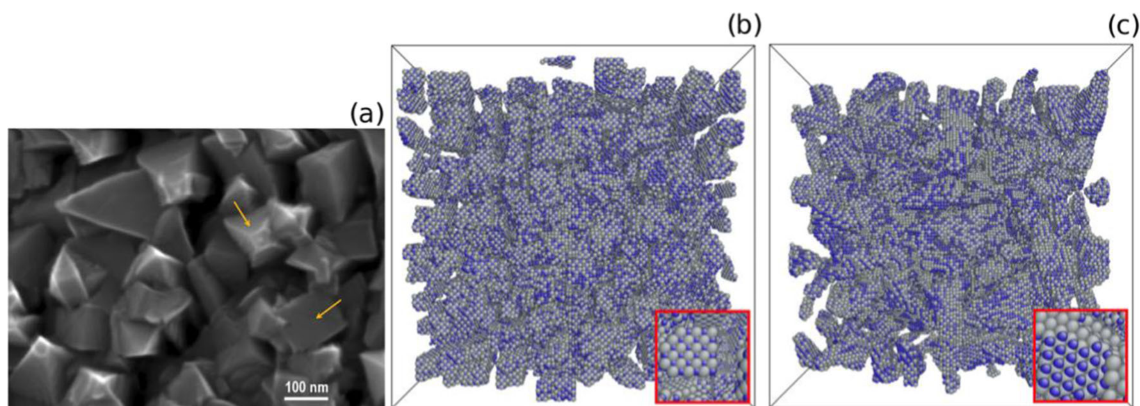

Fig. 18 Top-view SEM micrograph of a magnetron sputtered TiN film at 750 K (**a**), exhibiting faceted columns (arrows indicate local surfaces with either fourfold or threefold symmetry), compared with kMC simulation results obtained using two diffusion models. Insets in (**b**) and **c** are taken along the normal of the local surface, corresponding to (001)- and (111)-oriented surface.. Reprinted from Ref. [191]

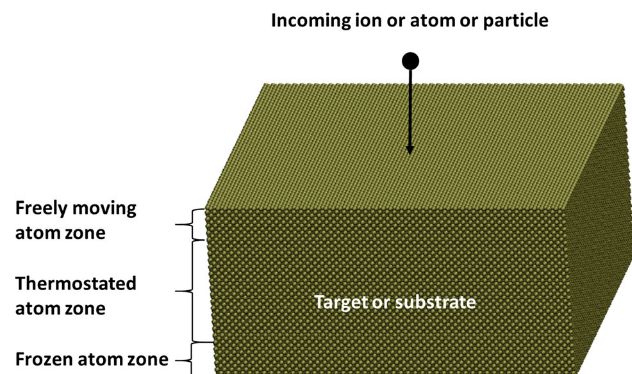

Fig. 19 Initial configuration of the simulation. Small spheres are substrate atoms at the crystal position. Amorphous or liquid substrates are also possible. The incoming species are at random location above the surface and are directed toward the surface with any possible angle consistent with experiments

Adsorption, and the motion on the surface or on the growing film or cluster, on the surface hence becomes a competition between the various processes, with E_{ik} the energy barrier defining the rate ki and thus the probability of an attempt to move to the next position [176]. A possible flowchart [117] displayed in Fig. 14 describes the simulation steps.

This method has been successful in reproducing (thick) thin film or cluster structure, composition and morphologies. For example, complex porous structures have been obtained and compared to experiments [188]. The origin of the growth of porous film has been elucidated using kMC and comparison with experiments (Figs. 15, 16).

On the other hand, reactions between species can be similarly included to simulate the growth of nitride, carbide, and oxide films [191, 192]. For example, the growth of a TiN film is simulated by fixing the possible places of Ti and N of a cubic B1 (NaCl-type) structure with a bulk lattice parameter $a0 = 0.424$ nm. The possible events are summarized in Fig. 17 [191]:

In this case, the total energy is calculated by considering interactions (barrier heights) of the nearest (Ti-N neighbors) and next nearest neighbor atoms (Ti–Ti and N–N neighbors). The energy values for different possible configurations are calculated, and the lowest one defines the occupied site.

This procedure allows the growth of TiN thin films to be studied, and various film structures can be compared with scanning electron microscopy (SEM). Two models, implementing two different ways for estimating energy barriers, were considered, leading to different film densities (Fig. 18).

kMC approaches are very powerful for describing growth in various conditions due to their flexibility in including various phenomena that may occur on different scales. They can address very large sized systems up to reactor scale [161]. The main limitation is the a priori knowledge of the different event rates that is necessary to run a kMC code. Such input data can be obtained by molecular models such as Quantum Chemistry (QC) approaches, among which Density Functional Theory is a flexible version dealing with different approximations aiming at reducing computational resources (time and memory requirements). Nevertheless, the computational cost is always very high. Fortunately, Molecular Dynamics simulations bridge the gap between the mesoscale (MC/kMC) and the molecular level of QC methods and open the way to successfully describing magnetron sputter deposition.

4.2 Molecular Dynamics models

In Molecular Dynamics (MD) simulations, the evolution of a system of N atoms (more generally species) is followed at the atomic/molecular level by solving the Newton equations of motion [195–200], in the general

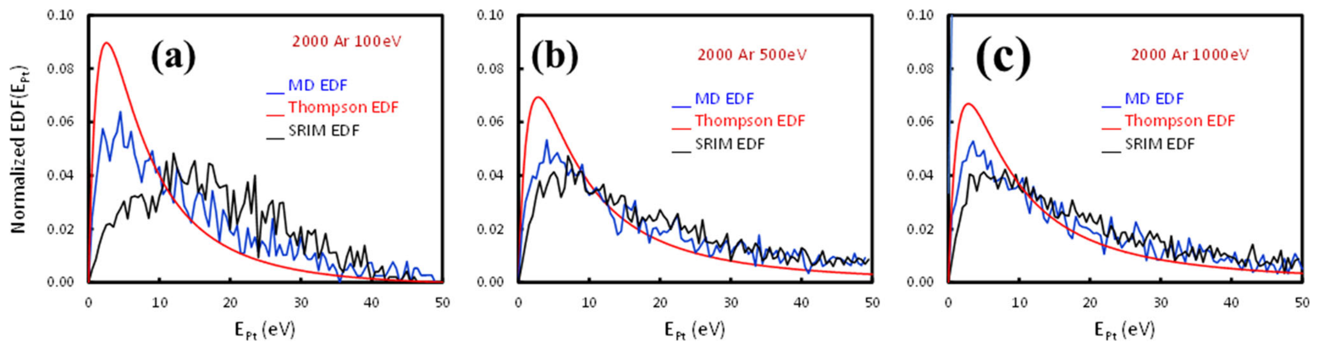

Fig. 20 Energy distribution function (EDF) of the sputtered Pt atoms. Ar ion kinetic energy of **a** 100 eV, **b** 500 eV **c** 1000 eV. Reprinted from Ref. [241]

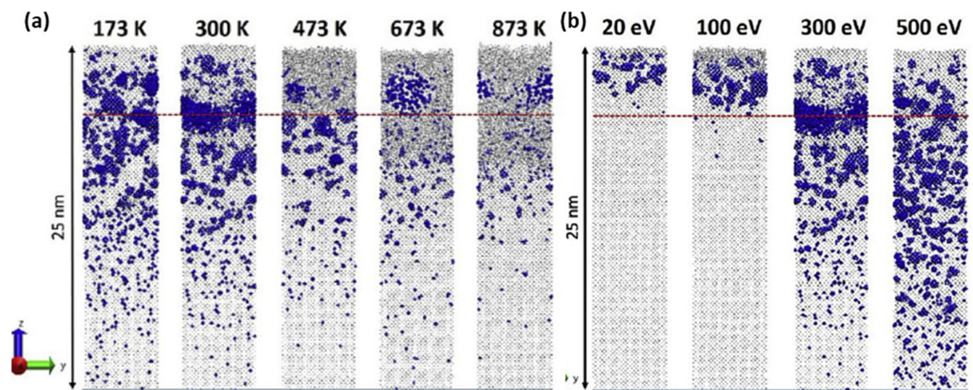

Fig. 21 Tungsten target temperature (**a**) and He kinetic energy (**b**) effects on helium retention. Blue spheres are helium atoms and gray dots are W atoms. Dots were chosen instead of spheres at the right size ratio to better display helium organization. Reprinted from Ref. [242]

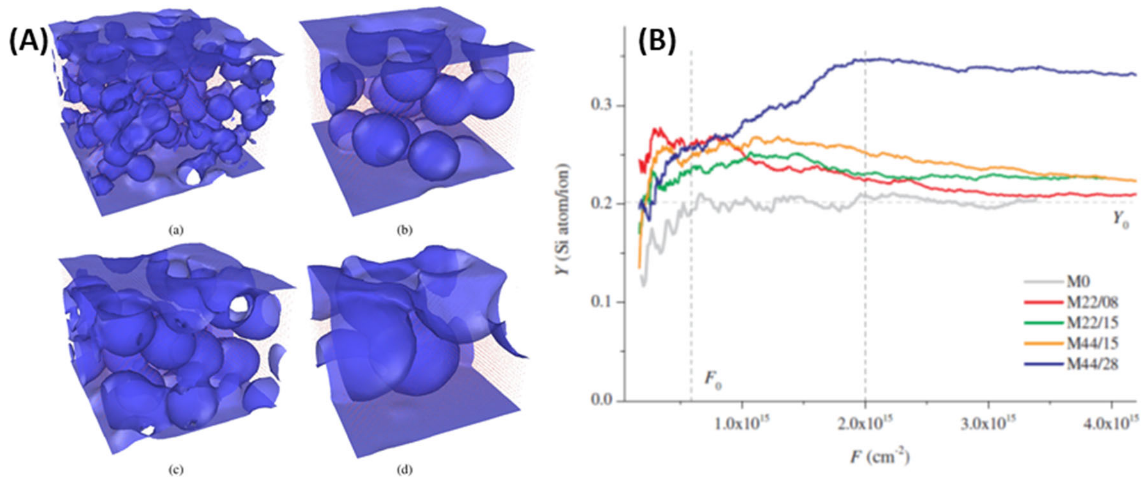

Fig. 22 **A** 3D images of four models with different pore radii and porosity: (a) M22/08; (b) M22/15; (c) M44/15; (d) M44/28. The nanoporous structure of models is represented by blue continuous surfaces. **B** Evolution of the sputtering yield by 200 eV Ar of the four nanoporous Si samples compared to crystalline Si (M0). Reprinted from [244]

form:

$$m_i \frac{d^2\vec{r}_i(t)}{dt^2} = \vec{F}_i = -\vec{\nabla} V(\vec{r}_1(t), \vec{r}_2(t), \cdots, \vec{r}_N(t)) \tag{16}$$

where $\vec{r}_i(t)$ is the position of atom i at time t with mass m_i, and V is the interaction potential between all N involved species. These equations only require the knowledge of two initial conditions, positions, and velocities at initial time $t = 0$, and of the interactions between all species at every time. The initial positions refer to geometry/topology of particles at the beginning of the simulation. Velocities are (randomly) selected from a velocity distribution that is consistent with the phenomena under study, for example selected from a Maxwell–Boltzmann distribution,

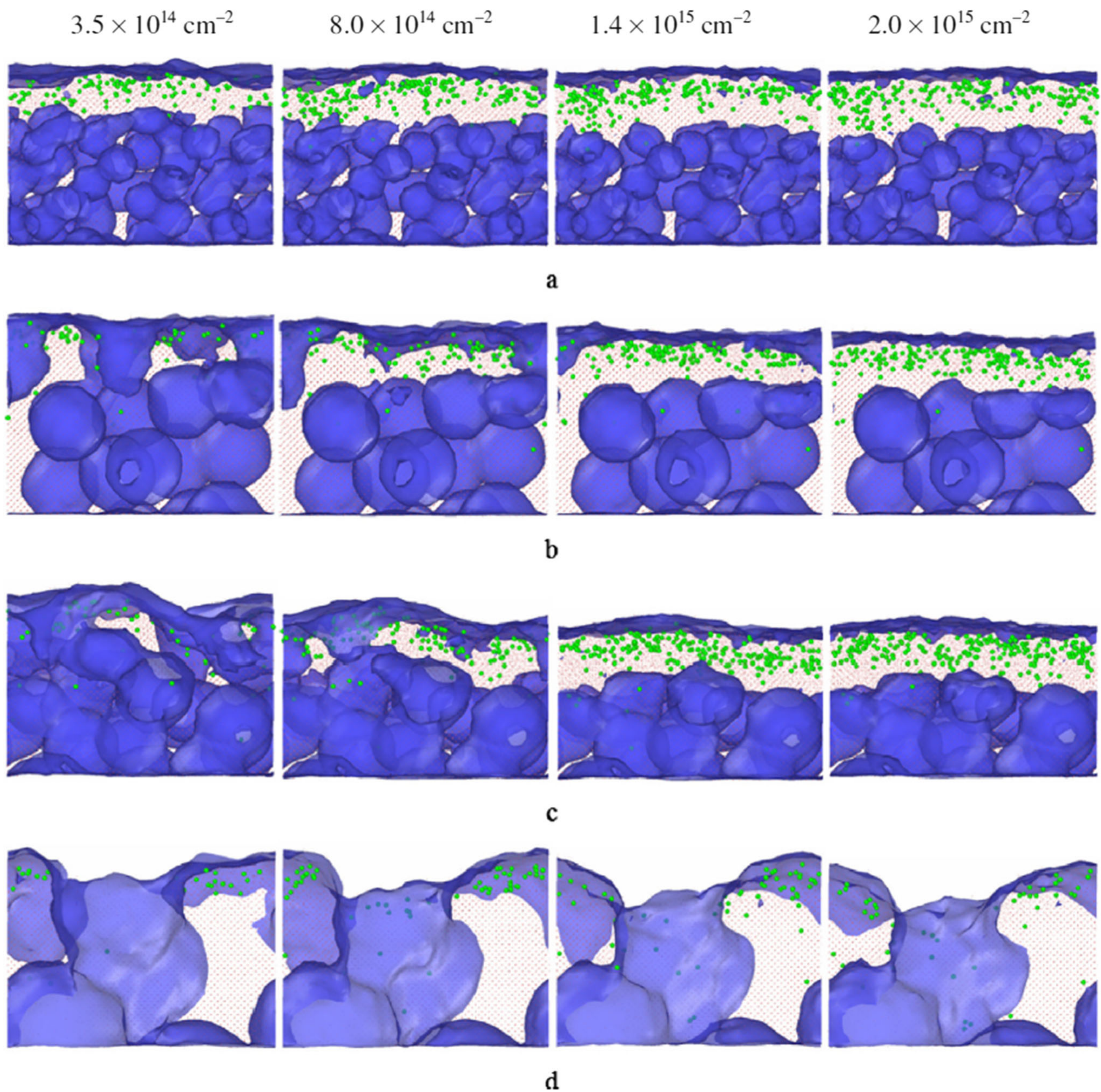

Fig. 23 Side views of the nanoporous models obtained at different ion fluences (given on top of the figure): **a** 22% porosity and pore radius 0.8 nm; **b** 22% porosity and pore radius 1.5 nm; **c** 44% porosity and pore radius 1.5 nm; **d** 44% porosity and pore radius 2.8 nm. Implanted Ar atoms are shown with green circles, and blue surfaces represent the nanoporous structure. White areas represent the empty regions. Reprinted from Ref. [246]

from any relevant velocity distribution obtained from experiment (mass spectrometry for example), or from any other simulations dedicated to determining velocity or kinetic energy distributions such as those described above. The most difficult part concerns the interactions. Often, force fields are defined in a semi-empirical functional form including pair interactions, three-body and many-body interactions [54, 195, 196, 201–206]. Comparison between different force fields has been conducted [204–206], but not extensively. Both the quality of the potential and the computer time required when using complex many-body and targeted phenomena drive the choice of the force fields. Moreover, very recently machine learning-based force fields emerged in the field of sputtering studies [207].

Leapfrog and Velocity Verlet algorithms can be used [195, 196] to solve the equation of motion (20). The latter ensures the lower numerical error propagation.

It is assumed that positions $\vec{r}_i(t)$, velocities $\vec{v}_i(t)$ and accelerations $\vec{a}_i(t) = -\frac{\vec{F}_i(t)}{m_i}$ are known at time t, the velocities $\vec{v}_i\left(t + \frac{dt}{2}\right)$ at time t + dt/2 can be evaluated by: $\vec{v}_i\left(t + \frac{dt}{2}\right) = \vec{v}_i(t) + \vec{a}_i(t)\frac{dt}{2}$. Next, the new positions at time $t + dt$ can be estimated as $\vec{r}_i(t + dt) = \vec{r}_i(t) + \vec{v}_i\left(t + \frac{dt}{2}\right)$. Accelerations at t + dt $\vec{a}_i(t + dt) = \vec{a}_i[\vec{r}_i(t + dt)]$ can be calculated and the velocities at time t + dt can be determined: $\vec{v}_i(t + dt) = \vec{v}_i\left(t + \frac{dt}{2}\right) + \vec{a}_i(t + dt)\frac{dt}{2}$. This is repeated at each time step.

Molecular Dynamics simulations are used like Monte-Carlo-based methods for sputtering [208–245], transport (to a lesser extent) [246–256], deposition and film growth [257–305].

The main interest is that there is no a priori prescription on the rate constant. In fact, MD is a tool for finding rates that can be input to MC methods. Such outputs will only be dependent on the force fields. When the force fields are analytically defined, even when many-body interactions come into play, the calculations are faster. Nevertheless, calculating force at each time step remains quite time-consuming. Another limitation is that the high kinetic energies of both sputtering ions and sputtered atoms require very small timesteps in order to solve the Newton equations of motion, for instance 0.1 fs [195]. Therefore, nanosecond time calculations require 10^7 timesteps. A problem that arises in MD simulation is the huge species flux difference between experiments and simulation. Typical experimental values can be on the order of 10^{15} cm^{-2} s^{-1}, i.e. 10 nm^{-2} s^{-1}, while for MD simulations, they are on the order of 1 (10 nm^{-2}) ps^{-1}, i.e. 10^{10} nm^{-2} s^{-1}. The use of high flux in MD results in a high energy release to the substrate. To avoid this, the target or substrate can be thermostated with a relaxation time on the order of a few ps, which corresponds to phonon relaxation in solids. Thus, between two impacts, the surface recovers its initial temperature or nearly so. By releasing atoms or ions at time intervals on the order of thermal relaxation times, high incoming fluxes can then be used. There are many ways for implementing thermostats in MD simulations, such as Berendsen, Nosé-Hoover, Langevin, etc. [228–231]. A simulation box is designed as follows: a periodic solid (liquid) is periodic in xy mimicking an infinite target/substrate and thick enough in the z direction to prevent diffusing species from crossing the sample. The first few layers at the bottom of the simulated solid (or liquid) are motionless so as to mimic infinite solids in the vertical direction and to prevent motion of the substrate/target in the$z$ direction. An intermediate zone is thermostated, while a few top layers are left free to move. Finally, incoming ions of atoms start from a height above the surface that is slightly larger than the highest cutoff radius, allowing smooth entry in the interaction zone. An illustration of such a design is given in Fig. 19.

4.2.1 MD simulations of sputtering

MD simulations of sputtering are realized by releasing a statistically significant number of ions toward the target. In order to be as close as possible to the experiments, the ion positions are randomly selected above the simulated target, while velocities are deduced from the kinetic energy eV_b, where V_b is the cathodic fall potential at the biased target. These velocities can be normal to the target surface, but for a more realistic approach, a slight angle of incidence can be accounted for.

Since ions are neutralized at the target surface, they can be treated as fast neutrals [238, 239].

Using the procedure described above, incoming ions will develop the collision cascade similar to Fig. 4. Thus, sputtering yields, retention rates and energy distribution functions can be calculated and compared to other models such as SRIM and theories. As illustration, Fig. 20 compares the energy distribution of sputtered Pt at different sputtering energies [239]. At high energy sputtering, MD simulations and SRIM are close since MD and the Thompson formula are closer at low energy sputtering.

Since SRIM always calculates the sputtering features with a virgin target, the differences with MD can be attributed to the fact that MD accounts for a material that evolves in the course of the sputtering. Since at high energy the two simulations are close, this means that the approximation of binary collisions in an amorphous solid is valid. Some specific phenomena have been addressed by MD such as preferential sputtering in alloys [242]: it is found that the lighter and the weaker bound species are sputtered preferentially. Retention of the sputtering ion in the target has drawn attention, especially for the application in Helium sputtering of fusion wall materials [240, 242 and references therein]. Helium implantation results in the growth of He bubbles that produce various surface morphologies and structures induced by swelling and flaking. Moreover, it was found that MD simulations are consistent with experiments, regarding dose, energy and temperature effects. A typical incoming He energy and tungsten temperature dependence of the implanted He distribution is displayed in Fig. 21 [240]

The sputtering of complex (porous) materials [242–244] is also of interest since bombarding a soft material is expected to modify sputtering rates and sputtered species energy and angle distribution.

A nanoporous structure increases sputtering rates due to local curvature effects, as shown in Fig. 22. Moreover, the non-monotonic nature of the sputtering yields versus Ar dose is attributed to the morphology change in the porous structure, as shown in Fig. 23.

4.2.2 MD simulations of sputtered atom transport

Simulating the transport of sputtered atoms using MD is not straightforward since the gas between the target and the substrate is highly diluted. A 1 atm gas gives

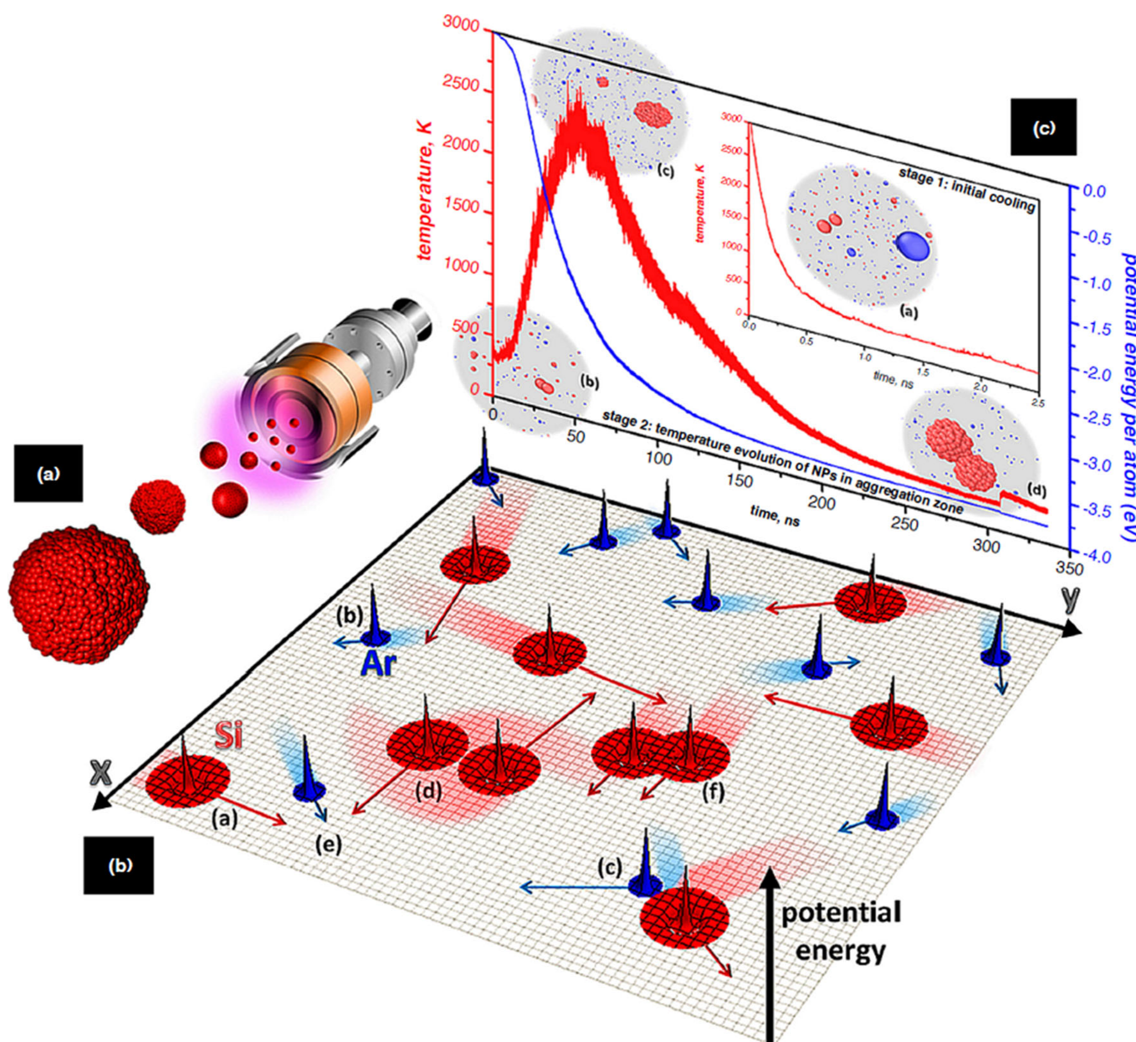

Fig. 24 **a** Illustration of pure-Si cluster growth from a single-target magnetron sputtering source. **b** Schematic representation of an MD simulation box, containing Si and Ar atoms, represented by red and blue potential energy functions (instances **a** and **b**, respectively). Atom velocity vectors are indicated by arrows. Instance **c** depicts a Si and Ar system post-collision (note the velocity exchange, implying cooling of the Si atom and heating of the Ar atom). Instance **d** shows the temporary attraction of two Si atoms not resulting in bond formation. In contrast, instance **e** indicates an imminent three-body collision that may result in bond formation. Instance **f** depicts a stable Si dimer. **c** Temperature and potential energy evolution during nucleation and growth of a Si nanoparticle (500 Si and 1500 Ar atoms in the MD box). The inset focuses on cooling during the initial 2.5 ns. MD visualization snapshots designate four steps of the growth mechanism. Reprinted from Ref. [255]

a density of 2 10^{-2} nm^{-3}. Assuming a 10 × 10 × 110 nm^3 simulation box, there will be only 20 gas atoms in the simulation cell. Therefore, this cannot represent the reality of collisional transport to the substrate.

An alternative is to use an MC step as described in Sect. 4.1.2 to determine the velocity of the sputtered atoms at the substrate surface and use it as an initial condition for a further MD simulation of the growth with these incoming atoms. A faster approach is to evaluate analytically the change in the sputtered atom energy distribution function when passing through a gas at temperature T_g and pressure P [52, 53, 233]. The final energy E_f of an atom traveling a distance $d_{T\text{-}S}$ between the target and the substrate is given by:

$$E_F = (E - k_B T_g)\exp[n\ln(E_f/E_i)] + k_B T_g \quad (17)$$

E_f/E_i = 1-γ/2 is the ratio of energies after and before a collision, $\gamma = 4\frac{m_i m_t}{(m_i+m_t)^2}$ [53], and $n = \mathrm{d}P\sigma/k_B T_g$, σ being the collision cross section between the sputtered target atom and the gas atom. E_i is the energy of the sputtered particles as they leave the target, n is the number of collisions that take place in the gas, d is the distance traveled. To calculate the energy loss (E_f) of sputtered atoms with the gas atoms during the flight

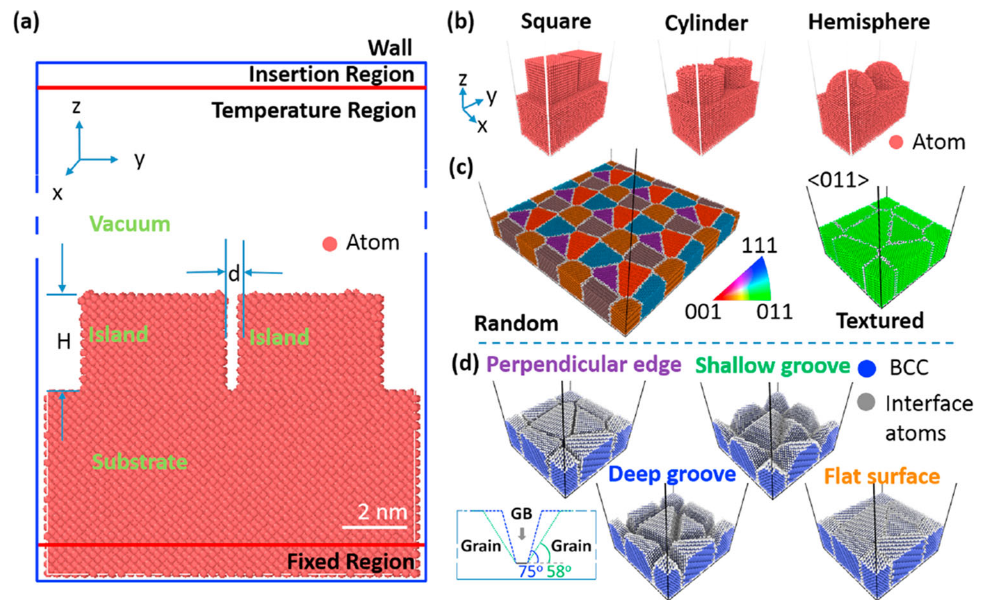

Fig. 25 **a** A sketch of the MD model, **b** single crystalline island model, **c** polycrystalline island model with random and ⟨0 1 1⟩ texture and **d** polycrystalline islands with different surface morphologies. The insert sketch helps the reader to find the slope of island grains for the deep groove model and the shallow groove model. The slope angles for the deep and the shallow groove models are 75° and 58°, respectively. Reprinted from Ref. [302]

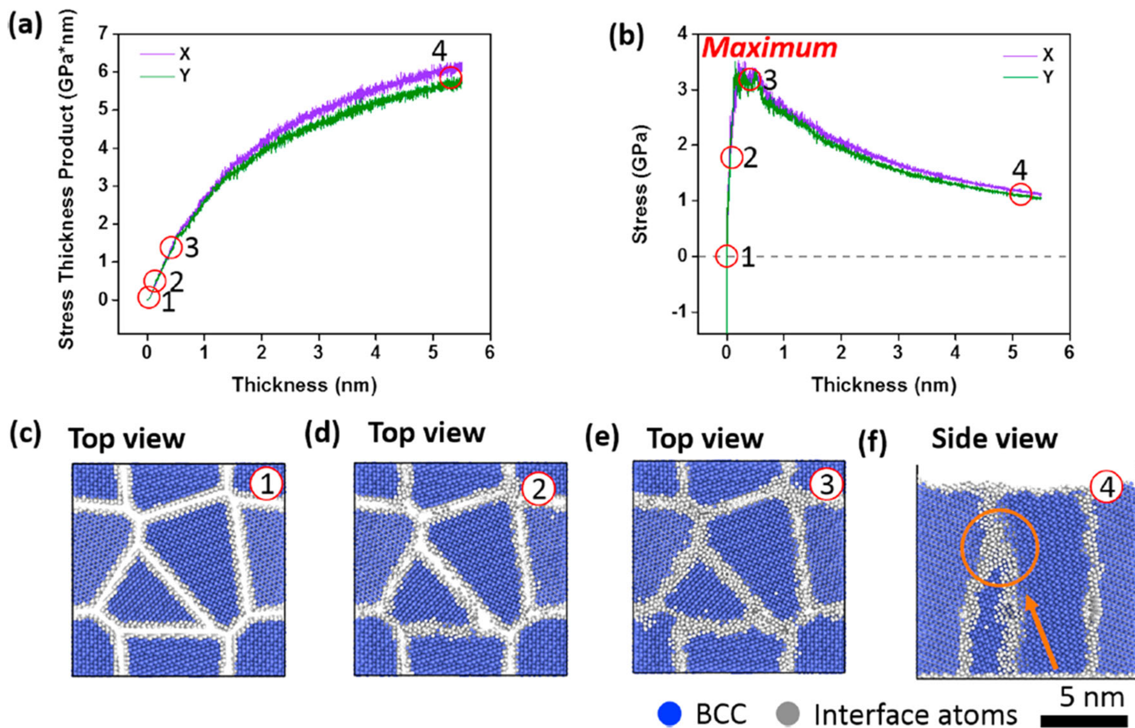

Fig. 26 **a** Stress and thickness products; **b** Stress varying with film thickness when 5 eV tungsten atoms are deposited onto the surface of a perpendicular edge island; **c**–**e** Three 2 nm top view slices, near the surface of the substrate were chosen to show the coalescence process. **f** One 2 nm side view slice to illustrate grain growth during deposition. The numbers represent the position where the slices were selected to calculate plots (a) and (b). Reprinted from Ref. [302]

toward the substrate, a Maxwell–Boltzmann (MB) distribution at T_{g} is used for the velocity distribution of the gas. Because we search for the complete energy distribution $F(E_{\mathrm{f}})$ of sputtered atoms, for each E_{g} in the MB gas distribution, the energy loss is calculated for a fixed value of the kinetic energy E of a sputtered atom. This is repeated for each energy value of the distribution and weighted by the collision probability, which is simply the convolution of $F(E_{\mathrm{f}})$ and the MB distribution at T_{g}. [52]. Initial kinetic energies can be obtained from such a distribution using a rejection method, and velocities can be deduced.

Another way is to scale down the reactor size to an MD simulation box. This is achieved by stating that the collision number along the travel path to the substrate

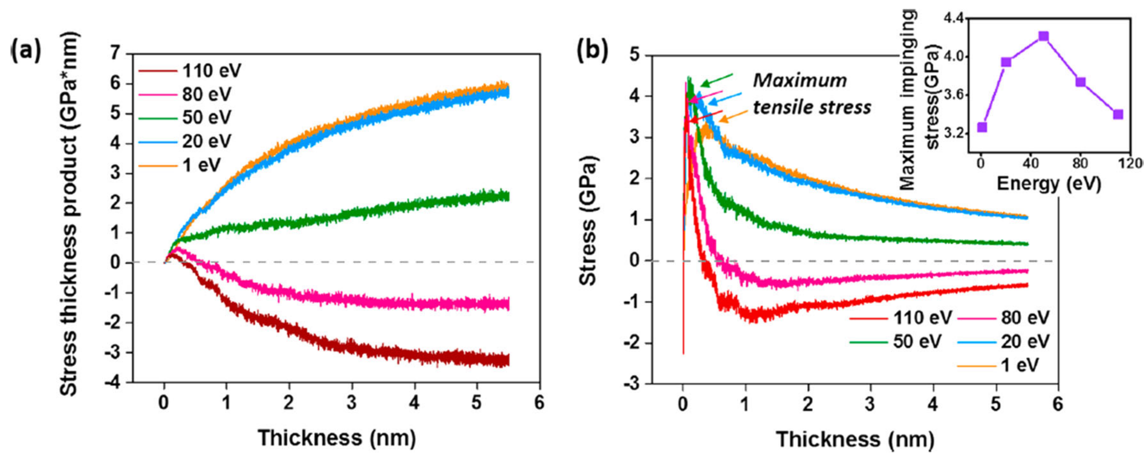

Fig. 27 **a** Stress and thickness products and **b** stress varying with film thickness when 1 eV, 20 eV, 50 eV, 80 eV, and 110 eV tungsten atoms deposited onto the surface of a perpendicular edge islands. The maximum impinging tensile stress for different injection energies are plotted in inset in (**b**). Reprinted from Ref. [302]

in the simulation box is the same as in the experimental sputtering reactor [250, 255]. Equating the collision number in the simulation box (index sim) and in the reactor (index exp) leads to the relation

$$P_{\text{exp}} d_{\text{exp}} = P_{\text{sim}} d_{\text{sim}} \tag{18}$$

Note that the simulation box volume can be written as $V_{\text{sim}} = S_{\text{sim}} d_{\text{sim}}$ where S_{sim} is the area normal to d_{sim}. If d_{sim} is along the z axis then S_{sim} is in the xy plane. Using $P_{\text{sim}} = \frac{N_{\text{sim}}}{V_{\text{sim}}} \cdot k_B T_g$, with N_{sim} being the number of atoms in the simulation box, Eq. (22) can be rewritten as:

$$N_{\text{sim}} = \frac{P_{\text{exp}}}{k_B T_g} \cdot S_{\text{sim}} \cdot d_{\text{exp}} \tag{19}$$

which does not depend on d_{sim}. Nevertheless, d_{sim} can be calculated keeping in mind that the species in the gas/plasma phase should not be closer than the largest interaction cutoff r_{cut} used in the simulations. The distance l between gas/plasma phase species can thus be estimated as:

$$l = \left[\frac{N_{\text{sim}}}{S_{\text{sim}} \cdot d_{\text{sim}}}\right]^{\frac{1}{3}} > r_{\text{cut}} \text{ and thus}, d_{\text{sim}} > \frac{N_{\text{sim}}}{S_{\text{sim}}} \cdot r_{\text{cut}}^3 \tag{20}$$

Therefore, the correct number of species in the simulation box can be deduced in order to match experimental conditions. This makes it possible to describe a full sputtering/transport/deposition on a substrate system using only MD simulations [250, 255].

Such an approach is relevant for the in-flight growth of nanoparticles during magnetron sputtering at high pressure in a gas aggregation source [246–256]. Such simulations have revealed the temperature evolution of the nanoparticles during growth as shown in Fig. 24. The ambient gas atom and the internal degrees of the growing nanoparticle share the excess bond energy of the growing nanoparticle. When the nanoparticles cease to grow, they are cooled by collision with the ambient gas, which is itself cooled by collision with the wall. This last step is simulated by thermostating the ambient gas with a relevant relaxation time.

4.2.3 MD simulations of sputter film growth

The first MD simulations of plasma sputtering deposition started in the late 1980s in two dimensions and addressed the effects of suprathermal energies on film structures as well as internal stress [257–259]. They were quickly followed by 3D simulations from the beginning of the 90 s, due to the increased capabilities of computers as well as the development of new many-body force fields (such as the embedded-atom method (EAM) and the modified embedded-atom method (MEAM)), well suited for studying metal sputtering and deposition [202]. In the meantime, pair potentials such as Buckingham or three-body Vashishta and Stillinger–Weber potentials [196] were used to study oxide and nitride compounds. As already mentioned, the use of such potentials needs to be carefully analyzed in view of the effects to be interpreted. For example, a phenomenon depending on the charge transfer would require a variable charge force field [201], while working at high temperature would require checking that the potential parametrization included high temperature materials properties, etc.

Simulating growth from sputtered particles (atoms, molecules, clusters) using MD requires the definition of the simulation box and the gas phase above the substrate surface. The box should be large enough to avoid boundary effects and is often periodic in the directions parallel to the surface (xy). The simplest way to build an MD growth simulation is to prepare a vapor of particles above the surface with velocities directed toward the surface. These velocities can be simply normal to the surface with values corresponding to the expected kinetic energy. A more elaborate scheme would select

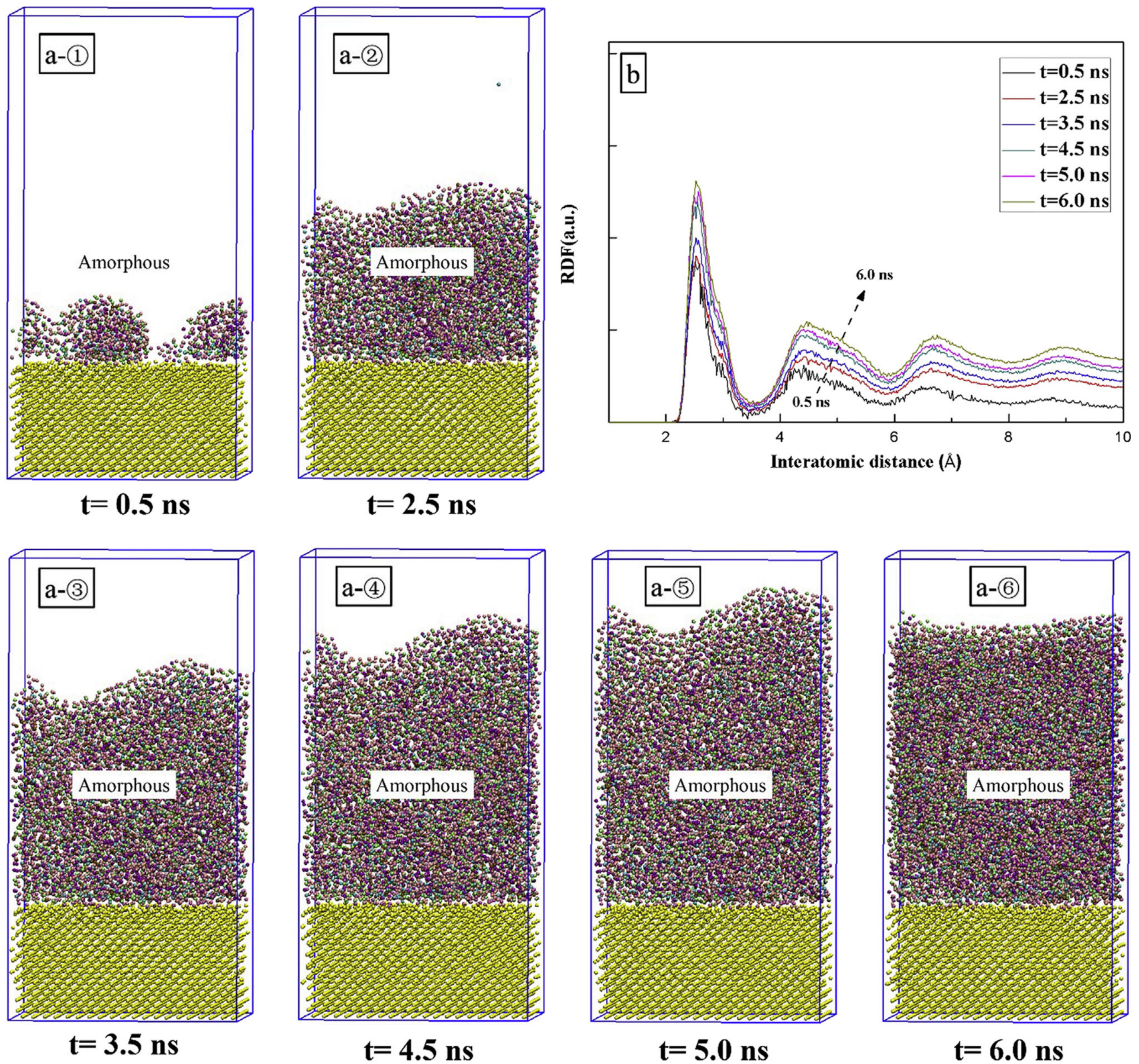

Fig. 28 Snapshots and RDF of $Al_2Co_9Cr_{32}Cu_{39}Fe_{12}Ni_6$ deposited on Si (100) substrate at different times **t**. (blue circle) Al, (violet circle) Co, (green circle) Cr, (pink circle) Cu, (brown circle) Fe, (purple circle) Ni, (yellow circle) Si. Reprinted from Ref. [295]

the velocity in a refined velocity distribution, obtained, for example, from energy resolved mass spectrometry.

Since microstructure development and stress in films are widely studied in experiments, this has led to numerous numerical studies in the past decade. They has been studied versus incoming ion energy, composition (for alloyed films), and temperature, often with the goal of comparing with experimental measurements and linking the atomic scales of MD to the experimental micron scales of topographies [270].

The total stress value of the film can be deduced from MD simulation via the velocities and force evaluations [276, 300]:

$$\sigma_{ij} = -\frac{1}{V}\sum_{\alpha\epsilon V}\left(M^{\alpha}v_i^{\alpha}v_j^{\alpha} + \frac{1}{2}\sum_{\beta\neq\alpha}F_i^{\alpha\beta}r_j^{\alpha\beta}\right), \text{where } V = \sum_{\alpha}V_{\alpha} \tag{21}$$

where σ_{ij} is the i, j component of the stress tensor for atom α (i, j = x, y, z), V^{α} is the atomic volume assigned to atom α, and $V\alpha = 1/\rho$, ρ is the atom number density per unit volume. M^{α} is mass, v_i^{α} is the i component of the velocity, v_j^{α} is the j component of the velocity of atom α. $F_i^{\alpha\beta}$ is the i component of the force on atom α due to atom β, and $r_j^{\alpha\beta}$ is the j component of the separation of atoms α and β.

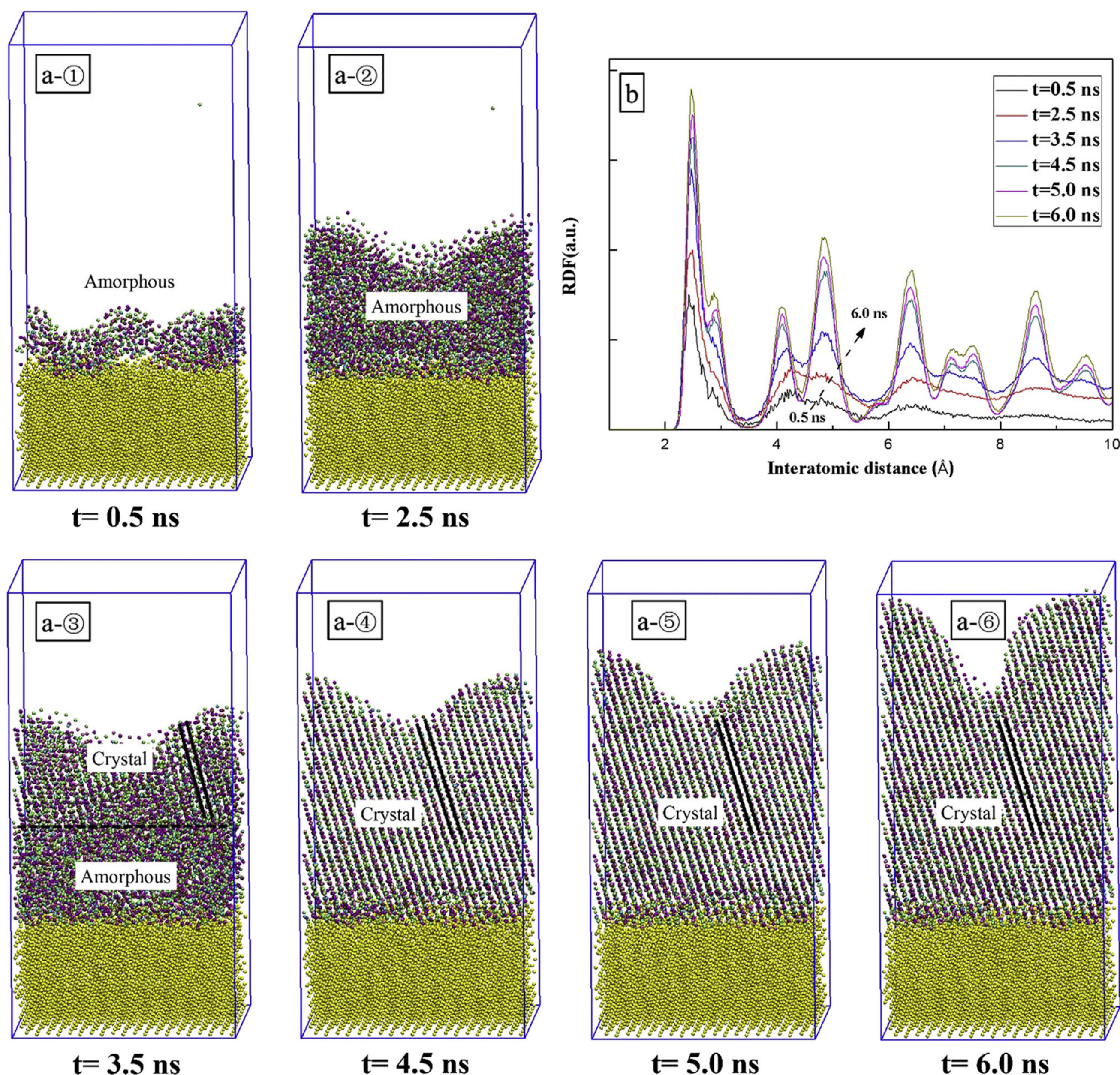

Fig. 29 Snapshots and RDF of $Al_3Co_{26}Cr_{15}Cu_{18}Fe_{20}Ni_{18}$ deposited on Si (100) substrate at different times. (blue circle) Al, (violet circle) Co, (green) Cr, (pink circle) Cu, (brown circle) Fe, (purple circle) Ni, (yellow circle) Si. Reprinted from Ref. [295]

For example, MD simulations of the growth stresses have been detailed as a function of various island textures, grain sizes, grain morphologies, deposition rates, and deposition energies [300].

Figure 25 displays the various initial configurations for studying stress generation of the various microstructures.

Evolution of the stress is calculated using realistic polycrystalline film. The elastic strain across multiple faces leads to a more homogeneous deformation. The stress state of the film is influenced by the surface morphology (Fig. 26).

Incoming atoms with higher energy transfer momentum into the film. This is known as an atomic peening effect, which induces a reduction in tensile stress or the generation of a compressive stress. The latter occurs for energies above 50 eV and for film thicker than 1 nm, as shown in Fig. 27.

Such a study is a very significant contribution to understanding the basic mechanism of microstructure and stress generation. More generally, this methodology can be easily reproduced for any thin film. Moreover, the use of free and well-documented LAMMPS software [306, 307] allows such mechanical simulations.

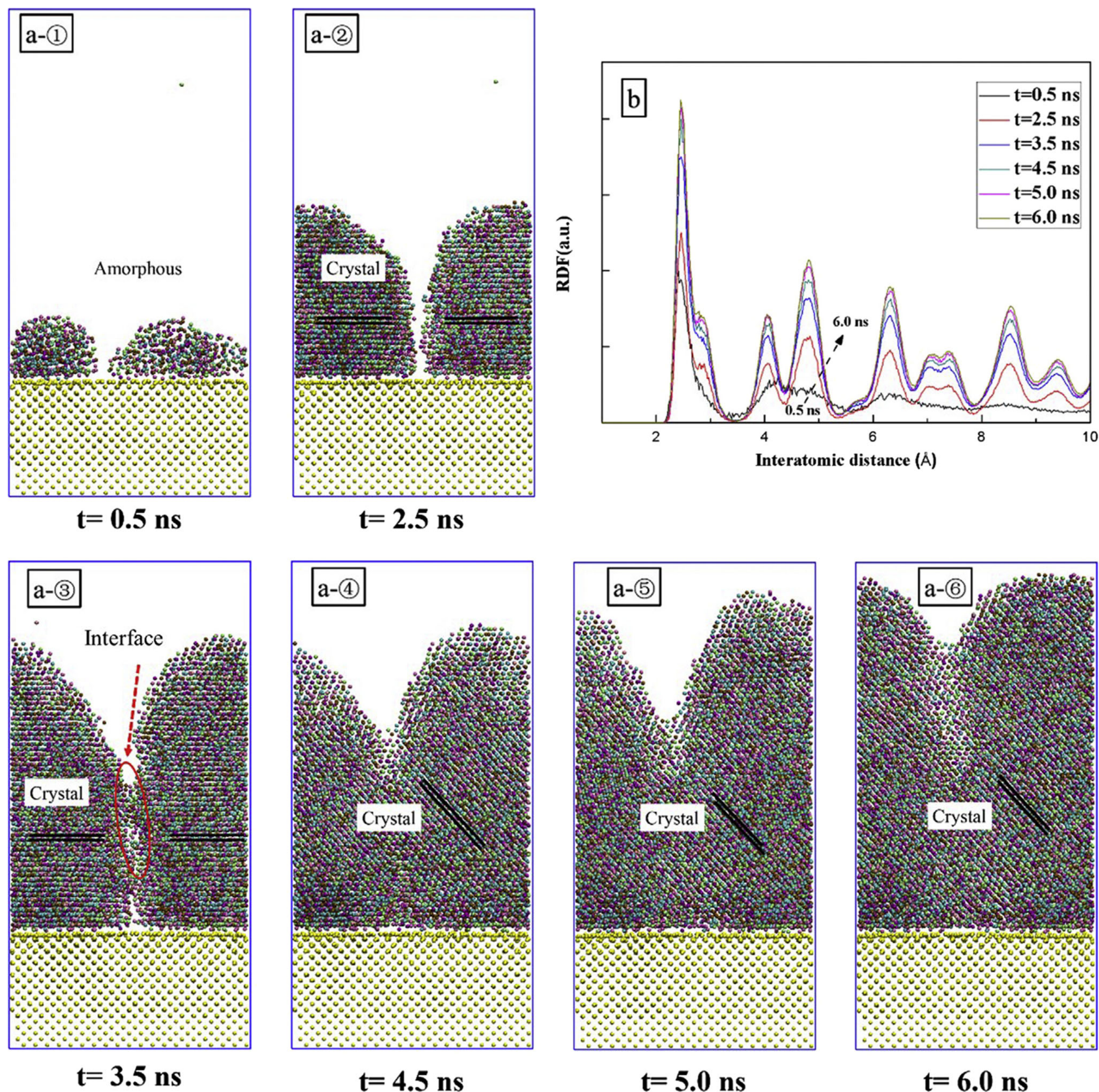

Fig. 30 Snapshots and RDF of $Al_{39}Co_{10}Cr_{14}Cu_{18}Fe_{13}Ni_6$ deposited on Si(100) substrate at different times. (blue circle) Al, (violet circle) Co, (green circle) Cr, (pink circle) Cu, (brown circle) Fe, (purple circle) Ni, (yellow circle) Si. Reprinted from Ref. [295]

The question that arises is the relevant box size needed for meaningful results that can be compared to experimental scales.

Multimetallic alloys have gained growing interest and among them high entropy alloys (HEA) have been investigated [308] due to their wide range of applications. They are also widely studied using MD since robust force fields are available, thus allowing direct comparison with experiments. They are also interesting modern techniques for high throughput simulations and developments based on machine learning (ML) models [308, 309]. ML techniques, and more generally Artificial Intelligence (AI), are intended to develop a data-based strategy to predict the structure, microstructure and properties of alloys which could minimize the number of experimental trials for alloy development. On the other hand, there is a great need of interaction potentials for oxide, nitride and carbide forms of HEA and ML and AI will certainly be called upon to play a central role in developing relevant interaction potentials. This will, in turn, enable MD and MC simulations of interest to be

Table 1 Comparison of MC/kMC and MD methods

	MC/ kMC Fully stochastic	MD
Statistical nature	Fully stochastic	Fully or partly deterministic
electron collisions	Yes (Sect. 3.). For kMC, yes too, but with increasing computer time	Not for a full plasma description. It comes from the mass difference between electron and atoms that will require extremely small timesteps. A workaround exists with reaxFF forcefield, but the electron mass is fixed to proton mass
System size dependence	There is no size dependence since only probabilities play a role both in the defining reaction rate and in calculating the associated time. It can treat different time scales simultaneously, when allowed by the fully stochastic nature of the processes involved	There is a size dependence. The reachable system size is dependent on the force evaluation. This limitation can be overcome using relevant periodic boundary conditions. Confidence in the statistical quantities deduced is dependent on the system size
Reachable time scales	All	Up to millisecond time scale, if acceleration techniques are implemented
Input parameters	Fully depends on input parameters such as rate coefficients	Depends only on the initial velocity and position conditions and forcefields. Able to calculate input parameters for MC/kMC simulations
Required CPU time	Depending on the system complexity, it is not CPU time-consuming	Depends on the force field, from CPU time-consuming to very time-consuming
Capability of addressing complex system	Depends on available data. Quantum chemistry (DFT) or MD simulations can provide missing data	Depends on available forcefields. Missing forcefields can be parametrized using quantum chemistry and machine learning methods

carried out for direct comparison to magnetron sputtering deposition simulations.

Composition effects, the kinetic energy of incident atoms, and temperature are parameters that are studied to determine the evolution of microstructure, morphologies, etc.

Figures 28, 29, 30 display the compositional effect on the microstructure evolution of HEA AlCoCrCuFeNi thin film alloys. When Al is the only low content element, the microstructure evolves from amorphous to crystalline during growth. At low contents of Al and Co, the microstructure remains amorphous throughout the deposition process with a high roughness while at high Al content the microstructure is always crystalline.

MD simulations are thus a very powerful technique for handling thin film deposition calculations and beyond this, the resulting properties. When starting such simulations, care should be taken on several points. The first one is the simulation box size that should be chosen sufficiently large to avoid frequent boundary recrossing. For systems with low atomic diffusion such as HEAs at moderate temperature, 10×10 Å^2 would be enough and would enable the deposition of "thick" films of a few tens of nm. When wishing to address polycrystalline films, large micron size grains are not reachable: 1 μm^3 of solid is around 10^{12} atoms, which is far from the possibilities of current computers even with low CPU time cost pair potentials. The second point is the choice of force field. The faster ones are the pair (2-body) potentials such as Lennard–Jones, Morse, Buckingham and three-body potentials reducible to sums of two-body potentials, but their interest is a primary approach and they are not recommended for production runs due to their poor ability to reproduce alloy properties. Many-body potentials such as EAM-MEAM have attracted considerable attention for thin metallic film growth since they are a good compromise between precision of the results and CPU cost. Using reactive force fields such as ReaxFF or COMB3 results in higher costs, but is only relevant for a small number of metal oxide, nitride, carbide and polymer compounds in thin film growth studies. Nevertheless, the CPU cost remains largely below quantum chemistry simulations coupled to MD, often called ab-initio

MD or first-principle MD simulations, for such deposition/growth studies. As mentioned previously, building robust interaction potentials with the assistance of AI tools appears to be a promising way.

4.3 Comparison between MC and MD methods

Table 1 provides a short comparative list of advantages and disadvantages of Monte-Carlo, kinetic Monte-Carlo, and Molecular Dynamics simulations methods for a quick view of benefits in using one of these methods.

5 Conclusion

This review spans almost all the ways of addressing sputtering, transport and subsequent film growth processes and some film properties. It presents the main features of the simulation methods investigated, coupled to some illustrative examples showing the interest of the method.

The theoretical analytical formula of sputtering and transport provides a first step for building an understanding of the processes involved.

Monte-Carlo models of plasma and transport are easy to handle with a reactor scale implementation capability. This is a major interest of MC methods. The cost is the knowledge of external parameters such as rate constants, which should be of high quality in order to ensure successful comparison with experiments and further, a good predictability capability. Regarding film growth, kMC methods are certainly the most powerful methods for handling growth phenomena up to micron scale grain sizes. Nevertheless, they are dependent on the set of input parameters that should be used. MD simulations, both for sputtering and film growth, can provide insight into all basic phenomena, including tribology, up to billion atom systems. Nevertheless, the robustness of the results largely depends on the quality of the force fields. When considering a multiscale approach, Molecular Dynamics can be a source of relevant data for MC, kMC and fluid (continuum) models.

Even if large sizes are not always required, multicore computers with parallel computing software are often required to handle meaningful simulations.

The abundant landscape of simulation approaches and tools provides relevant ways for finding a solution to each problem, provided the problem to be solved is clearly stated and modeled.

Acknowledgements This work was supported by SAFRAN Tech—Université d'Orléans – CNRS grant #LS 245305 and Conseil Regional du Centre – Val de Loire under Grant MATEX-202100145829. Elizabeth Rowley-Jolivet is gratefully acknowledged for English language editing.

Author contributions

PB wrote all drafts of the review article. All authors have read, discussed corrected, and edited all aspects of the review and have approved the final manuscript.

Data Availability Statement This manuscript has no associated data or the data will not be deposited. [Authors' comment: The paper is a review article and we have not generated any data.]

Declarations

Conflict of interest The authors declare no competing interests.

References

1. L. Xie, PhD thesis, https://tel.archives-ouvertes.fr/tel-00933201/document
2. P.J. Kelly, R.D. Arnell, Vacuum **56**, 159 (2000). https://doi.org/10.1016/S0042-207X(99)00189-X
3. K. Sarakinos, J. Alami, S. Konstantinidis, Surf. Coat. Technol. **204**, 1661 (2010). https://doi.org/10.1016/j.surfcoat.2009.11.013
4. D. Depla, S. Mahieu, R. Hull, R.M. Osgood, J. Parisi, J.M. Warlimont (eds.), *), Reactive Sputter Deposition* (Springer, Berlin Heidelberg, 2008)
5. A. Bogaerts, I. Kolev, and G. Buyle, In Reactive Sputter Deposition, ed. By D. Depla and S. Mahieu (Berlin: Springer-Verlag, 2008). p. 61
6. A. Anders, J. Appl. Phys. **121**, 171101 (2017). https://doi.org/10.1063/1.4978350
7. C.H. Townes, Phys. Rev. **65**, 319 (1944). https://doi.org/10.1103/PhysRev.65.319
8. D.E. Harrison, Phys. Rev. **102**, 1473 (1956). https://doi.org/10.1103/PhysRev.102.1473
9. E.B. Henschke, Phys. Rev. **106**, 737 (1957). https://doi.org/10.1103/PhysRev.106.737
10. D.T. Goldman, A. Simon, Phys. Rev. **111**, 383 (1958). https://doi.org/10.1103/PhysRev.111.383
11. W. Brandt, R. Laubert, Nucl. Inst. Methods **47**, 201 (1967). https://doi.org/10.1016/0029-554X(67)90431-4
12. G. Chapman, J. Kelly, Aust. J. Phys. **20**, 283 (1967). https://doi.org/10.1071/PH670283
13. P.D. Davidse, Vacuum **17**, 139–145 (1967). https://doi.org/10.1016/0042-207X(67)93142-9
14. M. W. Thompson, 377–414 (1968). https://doi.org/10.1080/14786436808227358
15. P. Sigmund, Phys. Rev. **184**, 383 (1969). https://doi.org/10.1103/PhysRev.184.383
16. P. Sigmund, Rev. Roum. Phys. **17**, 969 (1972)
17. K. Kanaya, K. Hojou, K. Koga, K. Toki, Jpn. J. Appl. Phys. **12**, 1297 (1973). https://doi.org/10.1143/JJAP.12.1297
18. H. Oechsner, Appl. Phys. **8**, 185–198 (1975). https://doi.org/10.1007/BF00896610
19. H.F. Winters, Adv. Chem. **158**, 1 (1976). https://doi.org/10.1021/ba-1976-0158.ch001

20. R. Kelly, Radiat. Eff. **32**, 91 (1977). https://doi.org/10.1080/00337577708237462
21. G. Betz, Surf. Sci. **92**, 283 (1980). https://doi.org/10.1016/0039-6028(80)90258-7
22. P. Sigmund, J. Vac. Sci. Technol. **17**, 396 (1980). https://doi.org/10.1116/1.570399
23. N. Matsunami, Y. Yamamura, Y. Itikawa, N. Itoh, Y. Kazumata, S. Miyagawa, K. Morita, R. Shimizu, Radiat. Eff. **57**, 15 (1981). https://doi.org/10.1080/01422448008218676
24. P. Sigmund, A. Oliva, G. Falcone, Nucl. Instrum. Methods Phys. Res. **194**, 541 (1982). https://doi.org/10.1016/0029-554X(82)90578-X
25. Z. Sroubek, Nucl. Instrum. Methods Phys. Res. **194**, 533 (1982). https://doi.org/10.1016/0029-554X(82)90577-8
26. Y. Yamamura, N. Matsunami, N. Itoh, Radiat. Eff. **68**, 83 (1982). https://doi.org/10.1080/01422448208226913
27. N.D. Lang, J.K. Nørskov, Phys. Scr. **T6**, 15 (1983). https://doi.org/10.1088/0031-8949/1983/T6/002
28. R. Kelly, D.E. Harrison, Mater. Sci. Eng. **69**, 449 (1985). https://doi.org/10.1016/0025-5416(85)90346-5
29. J.B. Malherbe, S. Hofmann, J.M. Sanz, Appl. Surf. Sci. **27**, 355–365 (1986). https://doi.org/10.1016/0169-4332(86)90139-X
30. G. Falcone, F. Gullo, Phys. Lett. A **125**, 432–434 (1987). https://doi.org/10.1016/0375-9601(87)90178-2
31. G. Falcone, Surf. Sci. **187**, 212 (1987). https://doi.org/10.1016/S0039-6028(87)80133-4
32. P. Sigmund, Nucl. Instrum. Methods Phys. Res. Sect. B **27**, 1 (1987). https://doi.org/10.1016/0168-583X(87)90004-8
33. G. Falcone, Sputtering transport theory: the mean energy. Phys. Rev. B **38**, 6398–6401 (1988). https://doi.org/10.1103/PhysRevB.38.6398
34. P.C. Zalm, Surf. Interface Anal. **11**, 1 (1988). https://doi.org/10.1002/sia.740110102
35. M.H. Shapiro, Nucl. Instrum. Methods Phys. Res. Sect. B **42**, 290–292 (1989). https://doi.org/10.1016/0168-583X(89)90722-2
36. G. Falcone, La Rivista del Nuovo Cimento della Societa Italiana di Fisica **13**, 1 (1990)
37. R.S. Mason, M. PichilingiJ, Phys. D: Appl. Phys. **27**, 2363 (1994). https://doi.org/10.1088/0022-3727/27/11/017
38. Z.L. Zhang, Nucl. Instrum. Methods Phys. Res. Sect. B **149**, 272–284 (1999). https://doi.org/10.1016/S0168-583X(98)00634-X
39. M. Stepanova, S.K. Dew, J. Vac. Sci. Technol. A **19**, 2805–2816 (2001). https://doi.org/10.1116/1.1405515
40. M. Stepanova, S.K. Dew, Nucl. Instrum. Methods Phys. Res. Sect. B **215**, 357–365 (2004). https://doi.org/10.1016/j.nimb.2003.09.013
41. G.K. Wehner, D. Rosenberg, J. Appl. Phys. (2004). https://doi.org/10.1063/1.1735395
42. G.N.V. Wyk, A.H. Lategan, Radiat. Eff. (2006). https://doi.org/10.1080/01422448208226917
43. R. Behrisch, W. Eckstein, Sputtering by Particle Bombardment: Experiments and Computer Calculations from Threshold to MeV Energies. (Springer Science & Business Media, 2007).
44. W.R. Grove, Philos. Trans. R. Soc. Lond. **142**, 87–101 (1852). https://doi.org/10.1098/rstl.1852.0008
45. Y. Yamamura, H. Tawara, At. Data Nucl. Data Tables **62**, 149–253 (1996). https://doi.org/10.1006/adnd.1996.0005
46. T. Ono, T. Kenmotsu, and T. Muramoto, In Reactive Sputter Deposition, ed. By D. Depla and S. Mahieu (Berlin: Springer-Verlag, 2008). p. 1
47. J.F. Ziegler, J.P. Biersack, U. Littmark, *The Stopping and Range of Ions in Solids* (Pergamon Press, New York, 1985)
48. J. Lindhard, M. Scharff, Phys. Rev. **124**, 128 (1961). https://doi.org/10.1103/PhysRev.124.128
49. T. Mousel, W. Eckstein, H. Gnaser, Nucl. Instrum. Methods Phys. Res. B **152**, 36–48 (1999). https://doi.org/10.1016/S0168-583X(98)00976-8
50. Y. Yamamura, T. Takiguchi, M. Ishida, Radiat. Eff. Defects Solids **118**, 237–261 (1991). https://doi.org/10.1016/S0168-583X(98)00976-8
51. T. Kenmotsu, Y. Yamamura, T. Ono, T. Kawamura, J. Plasma Fusion Res. **80**, 406 (2004). https://doi.org/10.1585/jspf.80.406
52. K. Meyer, I.K. Schuller, C.M. Falco, J. Appl. Phys. **52**, 5803–5805 (1981). https://doi.org/10.1063/1.329473
53. A. Gras-Marti, J.A. Valles-Abarca, J. Appl. Phys. **54**, 1071–1075 (1983). https://doi.org/10.1063/1.332113
54. P. Brault, E. Neyts, Catal. Today **256**, 3–12 (2015). https://doi.org/10.1016/j.cattod.2015.02.004
55. S. Berg, T. Nyberg, H.-O. Blom, C. Nender, *Handbook of Thin Film Process, Technology* (Institute of Physics Publishing, Bristol, UK, 1998)
56. S. Berg, T. Nyberg, Thin Solid Films **476**, 215 (2005). https://doi.org/10.1016/j.tsf.2004.10.051
57. S. Berg, H.-O. Blom, T. Larsson, C. Nender, J. Vac. Sci Technol. A **5**, 202 (1987). https://doi.org/10.1116/1.574104
58. S. Berg, T. Larsson, C. Nender, H.-O. Blom, J. Appl. Phys. **63**, 887 (1988). https://doi.org/10.1063/1.340030
59. H. Bartzsch, P. Frach, Surf. Coat. Technol. **142–144**, 192 (2001). https://doi.org/10.1016/S0257-8972(01)01087-8
60. V.A. Koss, J.L. Vossen, J. Vac. Sci. Technol. A Vac. Surf. Films **8**, 3791 (1990). https://doi.org/10.1116/1.576495
61. H. Ofner, R. Zarwasch, E. Rille, H.K. Pulker, J. Vac. Sci. Technol. A Vac. Surf. Films **9**, 2795 (1991). https://doi.org/10.1116/1.577202
62. H. Sekiguchi, T. Murakami, A. Kanzawa, T. Imai, T. Honda, J. Vac. Sci. Technol. A Vac. Surf. Films **14**, 2231 (1996). https://doi.org/10.1116/1.580051
63. S. Berg, T. Nyberg, and T. Kubart, In Reactive Sputter Deposition, ed. By D. Depla and S. Mahieu (Berlin: Springer-Verlag, 2008) p. 131
64. C. Costin, T.M. Minea, G. Popa, G. Gousset, Plasma Process. Polym. **4**, S960 (2007). https://doi.org/10.1002/ppap.200732307
65. S. Kadlec, Surf. Coat. Technol. **202**, 895 (2007). https://doi.org/10.1016/j.surfcoat.2007.06.043
66. I. Kolev, A. Bogaerts, J. Vac. Sci. Technol., A **27**, 20 (2008). https://doi.org/10.1116/1.3013856
67. A. Bogaerts, E. Bultinck, I. Kolev, L. Schwaederlé, K. Van Aeken, G. Buyle, D. Depla, J. Phys. D

Appl. Phys. **42**, 194018 (2009). https://doi.org/10.1088/0022-3727/42/19/194018
68. B. Zheng, Y. Fu, K. Wang, T. Tran, T. Schuelke, Q.H. Fan, Phys. Plasmas **28**, 014504 (2021). https://doi.org/10.1063/5.0029353
69. C.H. Shon, J.K. Lee, Appl. Surf. Sci. **192**, 258 (2002). https://doi.org/10.1016/S0169-4332(02)00030-2
70. A. Bogaerts, M. van Straaten, R. Gijbels, J. Appl. Phys. **77**, 1868 (1995). https://doi.org/10.1063/1.358887
71. A. Bogaerts, R. Gijbels, R.J. Carman, Spectrochim. Acta Part B **53**, 1679 (1998). https://doi.org/10.1016/S0584-8547(98)00201-8
72. T.M. Minea, J. Bretagne, G. Gousset, IEEE Trans. Plasma Sci. **27**, 94 (1999). https://doi.org/10.1109/27.763060
73. E. Shidoji, N. Nakano, T. Makabe, Thin Solid Films **351**, 37 (1999). https://doi.org/10.1016/S0040-6090(99)00151-0
74. J. Bretagne, C. Boisse Laporte, G. Gousset, O. Leroy, T.M. Minea, D. Pagnon, L. de Poucques, M. Touzeau, Plasma Sour. Sci. Technol. **12**, S33 (2003). https://doi.org/10.1088/0963-0252/12/4/318
75. C. Costin, L. Marques, G. Popa, G. Gousset, Plasma Sour. Sci. Technol. **14**, 168 (2005). https://doi.org/10.1088/0963-0252/14/1/018
76. T. Yagisawa, T. Makabe, J. Vac. Sci. Technol. A **24**, 908 (2006). https://doi.org/10.1116/1.2198866
77. I. Kolev, A. Bogaerts, J. Appl. Phys. **104**, 093301 (2008). https://doi.org/10.1063/1.2970166
78. E. Bultinck, A. Bogaerts, New J. Phys. **11**, 103010 (2009). https://doi.org/10.1088/1367-2630/11/10/103010
79. E. Bultinck, S. Mahieu, D. Depla, A. Bogaerts, New J. Phys. **11**, 023039 (2009). https://doi.org/10.1088/1367-2630/11/2/023039
80. C. Costin, T.M. Minea, G. Popa, G. Gousset, J. Vac. Sci. Technol. A **28**, 322 (2010). https://doi.org/10.1116/1.3332583
81. E. Bultinck, A. Bogaerts, Plasma Sour. Sci. Technol. **20**, 045013 (2011). https://doi.org/10.1088/0963-0252/20/4/045013
82. G. Kawamura, Y. Tomita, A. Kirschner, J. Nucl. Mater. **415**, S192 (2011). https://doi.org/10.1016/j.jnucmat.2010.09.057
83. T. Kozák, A. Dagmar Pajdarová, Journal of Applied Physics 110, 103303 (2011) https://doi.org/10.1063/1.3656446
84. A. Pflug, M. Siemers, C. Schwanke, B. Febty Kurnia, V. Sittinger, B. Szyszka, Materials Technology 26, 10 (2011). https://doi.org/10.1179/175355511X12941605982028
85. M.A. Raadu, I. Axnäs, J.T. Gudmundsson, C. Huo, N. Brenning, Plasma Sourc. Sci. Technol. **20**, 065007 (2011). https://doi.org/10.1088/0963-0252/20/6/065007
86. D. Depla, W.P. Leroy, Thin Solid Films **520**, 6337 (2012). https://doi.org/10.1016/j.tsf.2012.06.032
87. F.J. Jimenez, S.K. Dew, J. Vac. Sci. Technol. A **30**, 041302 (2012). https://doi.org/10.1116/1.4712534
88. F. Boydens, W.P. Leroy, R. Persoons, D. Depla, Thin Solid Films **531**, 32 (2013). https://doi.org/10.1016/j.tsf.2012.11.097
89. N. Brenning, D. Lundin, T. Minea, C. Costin, C Vitelaru, J. Phys. D: Appl. Phys. 46, 084005 (2013) https://doi.org/10.1088/0022-3727/46/8/084005
90. D. Depla, K. Strijckmans, R. De Gryse, Surf. Coat. Technol. **258**, 1011 (2014). https://doi.org/10.1016/j.surfcoat.2014.07.038
91. F.J. Jimenez, S.K. Dew, D.J. Field, J. Vac. Sci. Technol. A **32**, 061301 (2014). https://doi.org/10.1116/1.4894270
92. T.M. Minea, C. Costin, A. Revel, D. Lundin, L. Caillault, Surf. Coat. Technol. **255**, 52–61 (2014). https://doi.org/10.1016/j.surfcoat.2013.11.050
93. K. Strijckmans, D. Depla, J. Phys. D Appl. Phys. **47**, 235302 (2014). https://doi.org/10.1088/0022-3727/47/23/235302
94. J.T. Gudmundsson, D. Lundin, G.D. Stancu, N. Brenning, T.M. Minea, Phys. Plasmas **22**, 113508 (2015). https://doi.org/10.1063/1.4935402
95. K. Strijckmans, D. Depla, Appl. Surf. Sci. **331**, 185–192 (2015). https://doi.org/10.1016/j.apsusc.2015.01.058
96. J.T. Gudmundsson, D. Lundin, N. Brenning, M.A. Raadu, C. Huo, T.M. Minea, Plasma Sour. Sci. Technol. **25**, 065004 (2016). https://doi.org/10.1088/0963-0252/25/6/065004
97. A. Revel, T. Minea, S. Tsikata, Phys. Plasmas **23**, 100701 (2016). https://doi.org/10.1063/1.4964480
98. N. Brenning, J.T. Gudmundsson, M.A. Raadu, T.J. Petty, T. Minea, D. Lundin, Plasma Sour. Sci. Technol. **26**, 125003 (2017). https://doi.org/10.1088/1361-6595/aa959b
99. C. Huo, D. Lundin, J.T. Gudmundsson, M.A. Raadu, J.W. Bradley, N. Brenning, J. Phys. D Appl. Phys. **50**, 354003 (2017). https://doi.org/10.1088/1361-6463/aa7d35
100. D. Lundin, J.T. Gudmundsson, N. Brenning, M.A. Raadu, T. Minea, J. Appl. Phys. **121**, 171917 (2017). https://doi.org/10.1063/1.4977817
101. F. Moens, S. Konstantinidis, D. Depla, Front. Phys. **5**, 51 (2017). https://doi.org/10.3389/fphy.2017.00051
102. K. Strijckmans, F. Moens, D. Depla, J. Appl. Phys. **121**, 080901 (2017). https://doi.org/10.1063/1.4976717
103. J. Held, A. Hecimovic, A. von Keudell, V.S. von der Gathen, Plasma Sour. Sci. Technol. **27**, 105012 (2018). https://doi.org/10.1088/1361-6595/aae236
104. T. Kozák, J. Lazar, Plasma Sour. Sci. Technol. **27**, 115012 (2018). https://doi.org/10.1088/1361-6595/aaebdd
105. A. Revel, T. Minea, C. Costin, Plasma Sour. Sci. Technol. **27**, 105009 (2018). https://doi.org/10.1088/1361-6595/aadebe
106. S. Cui, Z. Wu, H. Lin, S. Xiao, B. Zheng, L. Liu, X. An, R.K.Y. Fu, X. Tian, W. Tan, P.K. Chu, J. Appl. Phys. **125**, 063302 (2019). https://doi.org/10.1063/1.5048554
107. D. Lundin, T. Minea, J. T. Gudmundsson, High Power Impulse Magnetron Sputtering: Fundamentals, Technologies, Challenges and Applications. (Elsevier, 2019).
108. B. Zheng, Z. Wu, S. Cui, S. Xiao, L. Liu, H. Lin, R.K.Y. Fu, X. Tian, F. Pan, P.K. Chu, IEEE Trans. Plasma Sci. **47**, 193 (2019). https://doi.org/10.1109/TPS.2018.2884475

109. T. Minea, T. Kozák, C. Costin, J. T. Gudmundsson, D. Lundin, in High Power Impulse Magnetron Sputtering, ed. By D. Lundin, T. Minea, J. T. Gudmundsson, (Amsterdam, Elsevier, 2020) p. 159
110. H. Eliasson, M. Rudolph, N. Brenning, H. Hajihoseini, M. Zanáška, M.J. Adriaans, M.A. Raadu, T.M. Minea, Plasma Sour. Sci. Technol. **30**, 115017 (2021). https://doi.org/10.1088/1361-6595/ac352c
111. M. Rudolph, H. Hajihoseini, M.A. Raadu, J.T. Gudmundsson, N. Brenning, T.M. Minea, A. Anders, D. Lundin, J. Appl. Phys. **129**, 033303 (2021). https://doi.org/10.1063/5.0036902
112. M. Rudolph, H. Hajihoseini, M.A. Raadu, J.T. Gudmundsson, N. Brenning, T.M. Minea, A. Anders, D. Lundin, Plasma Sour. Sci. Technol. **30**, 045011 (2021). https://doi.org/10.1063/5.0036902
113. T.E. Sheridan, M.J. Goeckner, J. Goree, J. Vac. Sci. Technol. A **8**, 30 (1990). https://doi.org/10.1116/1.577093
114. T.E. Sheridan, M.J. Goeckner, J. Goree, J. Vac. Sci. Technol. A **8**, 1623 (1990). https://doi.org/10.1116/1.576776
115. J.E. Miranda, M.J. Goeckner, J. Goree, T.E. Sheridan, J. Vac. Sci. Technol. A **8**, 1627 (1990). https://doi.org/10.1116/1.576777
116. M.J. Goeckner, J. Goree, T.E. Sheridan, IEEE Trans. Plasma Sci. **19**, 301 (1991). https://doi.org/10.1109/27.106828
117. J. Goree, T.E. Sheridan, Appl. Phys. Lett. **59**, 1052 (1991). https://doi.org/10.1063/1.106342
118. J. Li, Q. Chen, Z. Li, J. Phys. D: Appl. Phys. **28**, 681 (1995). https://doi.org/10.1088/0022-3727/28/4/010
119. J. Li, Q. Chen, Z. Li, J. Phys. D: Appl. Phys. **28**, 1121 (1995). https://doi.org/10.1088/0022-3727/28/6/014
120. J. Li, Q. Chen, W. Zhang, Z. Li, J.J. Pan, J. Phys. D: Appl. Phys. **29**, 1624 (1996). https://doi.org/10.1088/0022-3727/29/6/031
121. C. Heise, K. Lemke, M. Kock, Contrib. Plasma Phys. **37**, 431 (1997). https://doi.org/10.1002/ctpp.2150370505
122. Q.H. Fan, J.J. Gracio, L.Q. Zhou, J. Appl. Phys. **95**, 6017 (2004). https://doi.org/10.1063/1.1715133
123. S. Ido, K. Nakamura, Jpn. J. Appl. Phys. **32**, 5698 (1993). https://doi.org/10.1143/JJAP.32.5698
124. S. Ido, K. Nakamura, Vacuum **47**, 1035 (1996). https://doi.org/10.1016/0042-207X(96)00119-4
125. S. Ido, K. Nakamura, Jpn. J. Appl. Phys. **35**, 2302 (1996). https://doi.org/10.1143/JJAP.35.2302
126. M. Kashiwagi, S. Ido, Vacuum **53**, 33 (1999). https://doi.org/10.1016/S0042-207X(98)00417-5
127. S. Ido, M. Kashiwagi, M. Takahashi, Jpn. J. Appl. Phys. **38**, 4450 (1999). https://doi.org/10.1143/JJAP.38.4450
128. S. Ido, T. Suzuki, M. Kashiwagi, Jpn. J. Appl. Phys. **37**, 965 (1998). https://doi.org/10.1143/JJAP.37.965
129. E. Shidoji, M. Nemoto, T. Nomura, Y. Yoshikawa, Jpn. J. Appl. Phys. **33**, 4281 (1994). https://doi.org/10.1143/JJAP.33.4281
130. E. Shidoji, M. Nemoto, T. Nomura, J. Vac. Sci. Technol. A **18**, 2858 (2000). https://doi.org/10.1116/1.1312376
131. A. Lopp, C. Braatz, M. Geisler, H. Claus, and J. Trube, 45th Annual Technical Conference Proceedings of the Society of Vacuum Coaters, 170, (2002) , ISSN 0737–5921
132. Q.H. Fan, L.Q. Zhou, J.J. Gracio, J. Phys. D: Appl. Phys **36**, 244 (2003). https://doi.org/10.1088/0022-3727/36/3/305
133. T. Kubart, R. Novak, J. Valter, Czech. J. Phys. **54**, 1027 (2004)
134. G. Buyle, D. Depla, J. Haemers, W. De Bosscher, R. De Gryse, in SVC 48th Annual Technical Conference Proceedings (Denver, Colorado, 2005)
135. E.W. McDaniel, *Collision Phenomena in Ionized Gases* (Wiley, New York, 1964)
136. S.N. Nahar, J.M. Wadehra, Phys. Rev. A **35**, 2051 (1987). https://doi.org/10.1103/PhysRevA.35.2051
137. C.K. Birdsall, A.B. Langdon, *Plasma Physics via Computer Simulations* (Adam Hilger, Bristol, 1991)
138. I. Kolev, A. Bogaerts, Plasma Process. Polym. **3**, 127 (2006). https://doi.org/10.1002/ppap.200500118
139. G.A. Bird, Molecular gas dynamics and the direct simulation of gas flows, Oxf. Eng. Sci. Ser. (1994).
140. M. Turowski, M. Jupé, T. Melzig, P. Moskovkin, A. Daniel, A. Pflug, S. Lucas, D. Ristau, Thin Solid Films **592**, 240 (2015). https://doi.org/10.1016/j.tsf.2015.04.015
141. J.N. Brooks, D.N. Ruzic, J. Nucl. Mater. **176**, 278 (1990). https://doi.org/10.1016/0022-3115(90)90060-Z
142. J.P. Biersack, W. Eckstein, Appl. Phys. A **34**, 73 (1984). https://doi.org/10.1007/BF00614759
143. W. Möller, W. Eckstein, Nucl. Instrum. Methods Phys. Res. Sect. B **2**, 814 (1984). https://doi.org/10.1016/0168-583X(84)90321-5
144. W. Eckstein, J.P. Biersack, Appl. Phys. A **37**, 95 (1985). https://doi.org/10.1007/BF00618859
145. J.P. Biersack, Nucl. Instrum. Methods Phys. Res. Sect. B **27**, 21 (1987). https://doi.org/10.1016/0168-583X(87)90005-X
146. J.P. Biersack, S. Berg, C. Nender, Nucl. Instrum. Methods Phys. Res., Sect. B **59–60**, 21 (1991). https://doi.org/10.1016/0168-583X(91)95167-C
147. I. Strašík, M. Pavlovič, Radiat. Eff. Defects Solids **164**, 470–476 (2009). https://doi.org/10.1080/10420150902949910
148. R.E. Stoller, M.B. Toloczko, G.S. Was, A.G. Certain, S. Dwaraknath, F.A. Garner, Nucl. Instrum. Methods Phys. Res. Sect. B **310**, 75 (2013). https://doi.org/10.1016/j.nimb.2013.05.008
149. V.I. Shulga, Appl. Surf. Sci. **439**, 456–461 (2018). https://doi.org/10.1016/j.apsusc.2018.01.039
150. D.N. Ruzic, Nucl. Instrum. Methods Phys. Res. Sect. B **47**, 118–125 (1990). https://doi.org/10.1016/0168-583X(90)90019-Q
151. Y. Yamamura, Y. Mizuno, H. Kimura, Nucl. Instrum. Methods Phys. Res. Sect. B **13**, 393 (1986). https://doi.org/10.1016/0168-583X(86)90535-5
152. Y. Yamamura, C. Mössner, H. Oechsner, Radiat. Eff. **103**, 25 (1987). https://doi.org/10.1080/00337578708221239
153. Y. Yasunori, T. Wataru, Nucl. Instrum. Methods Phys. Res. Sect. B **29**, 461 (1987). https://doi.org/10.1016/0168-583X(87)90057-7
154. Y. Yamamura, K. Muraoka, Nucl. Instrum. Methods Phys. Res. Sect. B **42**, 175 (1989). https://doi.org/10.1016/0168-583X(89)90704-0

155. Yamamura, Y., Tawara, Atomic Data and Nuclear Data Tables 62, 149 (1996) https://doi.org/10.1006/adnd.1996.0005
156. Z. Li, T. Kenmotsu, T. Kawamura, T. Ono, Y. Yamamura, Nucl. Instrum. Methods Phys. Res. Sect. B **153**, 331 (1999). https://doi.org/10.1016/S0168-583X(98)01010-6
157. T. Kenmotsu, Y. Yamamura, T. Muramoto, N. Hirotani, Nucl. Instrum. Methods Phys. Res. Sect. B **228**, 369 (2005). https://doi.org/10.1016/j.nimb.2004.10.072
158. T. Motohiro, J. Vac. Sci. Technol A **4**, 189 (1986). https://doi.org/10.1116/1.573469
159. J. Emmerlich, S. Mráz, R. Snyders, K. Jiang, J.M. Schneider, Vacuum **82**, 867 (2008). https://doi.org/10.1016/j.vacuum.2007.10.011
160. Y. Yamamura, M. Ishida, J. Vac. Sci. Technol. A **13**, 101 (1995). https://doi.org/10.1116/1.579874
161. S. Mahieu, G. Buyle, D. Depla, S. Heirwegh, P. Ghekiere, R. De Gryse, Nucl. Instrum. Methods Phys. Res., Sect. B **243**, 313 (2006). https://doi.org/10.1016/j.nimb.2005.09.018
162. V. Abhilash, R. Balu, S. Balaji, S. Senthil Nathan, S. Mohan, Comput. Mater. Sci. **30**, 523 (2004). https://doi.org/10.1016/j.commatsci.2004.02.046
163. K.V. Aeken, S. Mahieu, D. Depla, J. Phys. D: Appl. Phys. **41**, 205307 (2008). https://doi.org/10.1088/0022-3727/41/20/205307
164. S. Kadlec, C. Quaeyhaegens, G. Knuyt, L. Stals, Surf. Coat. Technol. **97**, 633 (1997). https://doi.org/10.1016/S0257-8972(97)00375-7
165. K. Macàk, P. Macàk, U. Helmersson, Comput. Phys. Commun. **120**, 238 (1999). https://doi.org/10.1016/S0010-4655(99)00245-3
166. T. Motohiro, Y. Taga, Thin Solid Films **112**, 161 (1984). https://doi.org/10.1016/0040-6090(84)90493-0
167. A.M. Myers, J.R. Doyle, J.R. Abelson, D.N. Ruzic, J. Vac. Sci. Technol. A **9**, 614 (1991). https://doi.org/10.1116/1.577375
168. A.M. Myers, J.R. Doyle, D.N. Ruzic, J. Appl. Phys. **72**, 3064 (1992). https://doi.org/10.1063/1.351464
169. P.K. Petrov, V.A. Volpyas, R.A. Chakalov, Vacuum **52**, 427 (1999). https://doi.org/10.1016/S0042-207X(98)00326-1
170. G.M. Turner, I.S. Falconer, B.W. James, D.R. McKenzie, J. Appl. Phys. **65**, 3671 (1989). https://doi.org/10.1063/1.342593
171. O. Yamazaki, K. Iyanagi, S. Takagi, K. Nanbu, Jpn. J. Appl. Phys. **41**, 1230 (2002). https://doi.org/10.1143/JJAP.41.1230
172. K. Bobzin, R.P. Brinkmann, T. Mussenbrock, N. Bagcivan, R.H. Brugnara, M. Schäfer, J. Trieschman, Surf. Coat. Technol. **237**, 176 (2013). https://doi.org/10.1016/j.surfcoat.2013.08.018
173. R. Elsing, Surf. Coat. Technol. **49**, 132 (1991). https://doi.org/10.1016/0257-8972(91)90044-W
174. T. Heberlein, G. Krautheim, W. Wuttke, Vacuum **42**, 47 (1991). https://doi.org/10.1016/0042-207X(91)90076-U
175. A.P.J. Jansen, *An Introduction to Kinetic Monte Carlo Simulations of Surface Reactions* (Springer, 2012)
176. S. Lucas, P. Moskovkin, Thin Solid Films **518**, 5355 (2010). https://doi.org/10.1016/j.tsf.2010.04.064
177. N. Cheimarios, D. To, G. Kokkoris, G. Memos, A.G. Boudouvis, Front. Phys. **9**, 631918 (2021). https://doi.org/10.3389/fphy.2021.631918
178. G.H. Gilmer, H. Huang, C. Roland, Comput. Mater. Sci. **12**, 354 (1998). https://doi.org/10.1016/S0927-0256(98)00022-6
179. G. H. Gilmer, H. Huang, T. D de la Rubia, J. Dalla Torre, F. Baumann, Thin Solid Films 365, 189 (2000). https://doi.org/10.1016/S0040-6090(99)01057-3
180. H.N.G. Wadley, X. Zhou, R.A. Johnson, M. Neurock, Prog. Mater. Sci. **46**, 329 (2001). https://doi.org/10.1016/S0079-6425(00)00009-8
181. Y. Wang, in 31st Computers and Information in Engineering Conference (American Society of Mechanical Engineers Digital Collection, 2012) p; 241 https://doi.org/10.1115/DETC2011-48570
182. L.A. Zepeda-Ruiz, G.H. Gilmer, in Handbook of Crystal Growth (Second Edition) ed By T. Nishinaga, (Elsevier, 2015) p. 445 https://doi.org/10.1016/B978-0-444-56369-9.00010-1.
183. L.A. Zepeda-Ruiz, G.H. Gilmer, C.C. Walton, A.V. Hamza, E. Chason, J. Cryst. Growth **312**, 1183–1187 (2010). https://doi.org/10.1016/j.jcrysgro.2009.12.035
184. J. Cho, S.G. Terry, R. LeSar, C.G. Levi, Mater. Sci. Eng. A **391**, 390–401 (2005). https://doi.org/10.1016/j.msea.2004.09.015
185. J. Dalla Torre, G. H. Gilmer, D. L. Windt, R. Kalyanaraman, F. H. Baumann, P. L. OSullivan, J. Sapjeta, T. DíazdelaRubia, M. Djafari Rouhani, J. Appl. Phys. 94, 263–271 (2003). https://doi.org/10.1063/1.1579112
186. J. Dervaux, P.A. Cormier, P. Moskovkin, O. Douheret, S. Konstantinidis, R. Lazzaroni, S. Lucas, R. Snyders, Thin Solid Films **636**, 644–657 (2017). https://doi.org/10.1016/j.tsf.2017.06.006
187. F. Elsholz, E. Schöll, A. Rosenfeld, Phys. Status Solidi (b) **244**, 3639 (2007). https://doi.org/10.1002/pssb.200743257
188. V. Godinho, P. Moskovkin, R. Álvarez, J. Caballero-Hernández, R. Schierholz, B. Bera, J. Demarche, A. Palmero, A. Fernández, S. Lucas, Nanotechnology **25**, 355705 (2014). https://doi.org/10.1088/0957-4484/25/35/355705
189. L. Jablonka, P. Moskovkin, Z. Zhang, S.-L. Zhang, S. Lucas, T. Kubart, J. Phys. D Appl. Phys. **52**, 365202 (2019). https://doi.org/10.1088/1361-6463/ab28e2
190. Z. Liu, L. Yu, K.-L. Yao, X.-B. Jing, X. Li, X.-Z. Sun, J. Phys. D Appl. Phys. **38**, 4202 (2005). https://doi.org/10.1088/0022-3727/38/23/010
191. F. Nita, C. Mastail, G. Abadias, Phys. Rev. B **93**, 064107 (2016). https://doi.org/10.1103/PhysRevB.93.064107
192. R. Mareus, C. Mastail, F. Anğay, N. Brunetière, G. Abadias, Surf. Coat. Technol. **399**, 126130 (2020). https://doi.org/10.1016/j.surfcoat.2020.126130
193. L. Rosenthal, A. Filinov, M. Bonitz, V. Zaporojtchenko, F. Faupel, Contrib. Plasma Phys. **51**, 971–980 (2011). https://doi.org/10.1002/ctpp.201100034
194. R. Tonneau, P. Moskovkin, J. Muller, T. Melzig, E. Haye, S. Konstantinidis, A. Pflug, S. Lucas, J. Phys. D: Appl. Phys. **54**, 155203 (2021). https://doi.org/10.1088/1361-6463/abd72a

195. D. Graves, P. Brault, J. Phys. D **42**, 194011 (2009). https://doi.org/10.1088/0022-3727/42/19/194011
196. A. Omeltchenko, A. Nakano, K. Tsukura, R.K. Kalia, P. Vashishta, *in Advances in Metal and Semiconductors Clusters*, vol. 4 (JAI Press, Greenwich, CT, 1998), p.263
197. M.P. Allen, D.J. Tildesley, *Computer Simulations of Liquids* (Oxford University Press, New York, 1987)
198. J.M. Haile, *Molecular Dynamics Simulations* (Wiley, New York, 1992)
199. D.C. Rapaport, The Art of Molecular Dynamics Simulations (Cambridge: Cambridge University Press 1995)
200. D. Frenkel and B. Smit Understanding Molecular Simulation (Orlando, FL: Academic Press 2001)
201. E. Neyts, P. Brault, Plasma Process. Polym. **14**, 1600145 (2017). https://doi.org/10.1002/ppap.201600145
202. L. Xie, P. Brault, J.-M. Bauchire, A.-L. Thomann, L. Bedra, J. Phys. D: Appl. Phys. **47**, 224004 (2014). https://doi.org/10.1088/0022-3727/47/22/224004
203. A. Wucher, B.J. Garrison, Surf. Sci. **260**, 257 (1992). https://doi.org/10.1016/0039-6028(92)90040-D
204. B.J. Thijsse, T.P.C. Klaver, E.F.C. Haddeman, Appl. Surf. Sci. **231–232**, 29–38 (2004). https://doi.org/10.1016/j.apsusc.2004.03.207
205. D.E. Harrison, J. Appl. Phys. **52**, 1499–1508 (1981). https://doi.org/10.1063/1.329788
206. O.J. Tucker, D.S. Ivanov, L.V. Zhigilei, R.E. Johnson, E.M. Bringa, Nucl. Instrum. Methods Phys. Res. Sect. B **228**, 163–169 (2005). https://doi.org/10.1016/j.nimb.2004.10.040
207. L. Chen, A. Kaiser, M. Probst, S. Shermukhamedov, Nucl. Fusion **61**, 016031 (2020). https://doi.org/10.1088/1741-4326/abc9f4
208. G. Betz, R. Kirchner, W. Husinsky, F. Rüdenauer, H.M. Urbassek, Radiat. Effects Defects Solids Null **130**, 251–266 (1994). https://doi.org/10.1080/10420159408219788
209. Z. Insepov, I. Yamada, Nucl. Instrum. Methods Phys. Res. Sect. B **99**, 248–252 (1995). https://doi.org/10.1016/0168-583X(95)00322-3
210. G. Betz, W. Husinsky, Nucl. Instrum. Methods Phys. Res. Sect. B **102**, 281 (1995). https://doi.org/10.1016/0168-583X(95)80155-F
211. H. Gades, H.M. Urbassek, Nucl. Instrum. Methods Phys. Res. Sect. B **102**, 261 (1995). https://doi.org/10.1016/0168-583X(95)80152-C
212. J.E. Rubio, L.A. Marqués, M. Jaraíz, L.A. Bailón, J. Barbolla, Nucl. Instrum. Methods Phys. Res., Sect. B **102**, 301 (1995). https://doi.org/10.1016/0168-583X(95)80157-H
213. R.E. Johnson, M. Liu, J. Chem. Phys. **104**, 6041 (1996). https://doi.org/10.1063/1.471340
214. L.A. Marqués, J.E. Rubio, M. Jaraíz, L.A. Bailón, J.J. Barbolla, J. Appl. Phys. 81, 1488 (1997). https://doi.org/10.1063/1.363914
215. H.M. Urbassek, Nucl. Instrum. Methods Phys. Res. Sect. B **122**, 427 (1997). https://doi.org/10.1016/S0168-583X(96)00681-7
216. N.A. Kubota, D.J. Economou, S.J. Plimpton, J. Appl. Phys. **83**, 4055 (1998). https://doi.org/10.1063/1.367225
217. V.N. Samoilov, A.E. Tatur, N.A. Kovaleva, A.E. Kozhanov, Nucl. Instrum. Methods Phys. Res. Sect. B **153**, 319 (1999). https://doi.org/10.1016/S0168-583X(99)00216-5
218. E.M. Bringa, R.E. Johnson, M. Jakas, Phys. Rev. B **60**, 15107 (1999). https://doi.org/10.1103/PhysRevB.60.15107
219. E.E. Zhurkin, A.S. Kolesnikov, Nucl. Instrum. Methods Phys. Res., Sect. B **193**, 822 (2002). https://doi.org/10.1016/S0168-583X(02)00911-4
220. A.V. Krasheninnikov, K. Nordlund, E. Salonen, J. Keinonen, C.H. Wu, Comput. Mater. Sci. **25**, 427 (2002). https://doi.org/10.1016/S0927-0256(02)00318-X
221. E. Salonen, K. Nordlund, J. Keinonen, C.H. Wu, J. Nucl. Mater. **313–316**, 404 (2003). https://doi.org/10.1016/S0022-3115(02)01397-1
222. M.H. Shapiro, P. Lu, Nucl. Instrum. Methods Phys. Res. Sect. B **215**, 326 (2004). https://doi.org/10.1016/j.nimb.2003.08.036
223. C. Anders, H.M. Urbassek, R.E. Johnson, Phys. Rev. B **70**, 155404 (2004). https://doi.org/10.1103/PhysRevB.70.155404
224. K.O.E. Henriksson, K. Nordlund, J. Keinonen, Phys. Rev. B **71**, 014117 (2005). https://doi.org/10.1103/PhysRevB.71.014117
225. E. Despiau-Pujo, P. Chabert, D.B. Graves, J. Vac. Sci. Technol. A **26**, 274 (2008). https://doi.org/10.1116/1.2836408
226. AYu. Nikiforov, High Energy Chem. **42**, 235 (2008). https://doi.org/10.1134/S0018143908030090
227. B. Weidtmann, A. Duvenbeck, A. Wucher, Appl. Surf. Sci. **255**, 813 (2008). https://doi.org/10.1016/j.apsusc.2008.05.062
228. A. Ito, Y. Wang, S. Irle, K. Morokuma, H. Nakamura, J. Nucl. Mater. **390–391**, 183 (2009). https://doi.org/10.1016/j.jnucmat.2009.01.163
229. A.-P. Prskalo, S. Schmauder, C. Ziebert, J. Ye, S. Ulrich, Surf. Coat. Technol. **204**, 2081 (2010). https://doi.org/10.1016/j.surfcoat.2009.09.043
230. A. Duvenbeck, B. Weidtmann, A. Wucher, J. Phys. Chem. C **114**, 5715 (2010). https://doi.org/10.1021/jp905923w
231. O.A. Restrepo, A. Delcorte, J. Phys. Chem. C **115**, 12751 (2011). https://doi.org/10.1021/jp201183a
232. A. Duvenbeck, S. Hanke, B. Weidtmann, A. Wucher, Nucl. Instrum. Methods Phys. Res. Sect. B **269**, 1661 (2011). https://doi.org/10.1016/j.nimb.2010.11.082
233. C. Yan, Q.Y. Zhang, AIP Adv. **2**, 032107 (2012). https://doi.org/10.1063/1.4738951
234. F. Sefta, N. Juslin, K.D. Hammond, B.D. Wirth, J. Nucl. Mater. **438**, S493 (2013). https://doi.org/10.1016/j.jnucmat.2013.01.101
235. V. Cristaudo, C. Poleunis, B. Czerwinski, A. Delcorte, Surf. Interface Anal. **46**, 79 (2014). https://doi.org/10.1002/sia.5424
236. T. Aoki, J. Comput. Electron. **13**, 108 (2014). https://doi.org/10.1007/s10825-013-0504-5
237. M.L. Nietiadi, L. Sandoval, H.M. Urbassek, W. Möller, Phys. Rev. B **90**, 045417 (2014). https://doi.org/10.1103/PhysRevB.90.045417
238. L. Pentecoste, P. Brault, A.-L. Thomann, P. Desgardin, T. Lecas, T. Belhabib, M.-F. Barthe, T. Sauvage, J.

Nucl. Mat. **470**, 44 (2016). https://doi.org/10.1016/j.jnucmat.2015.12.017
239. P. Brault, S. Chuon, J.-M. Bauchire, Front. Phys. **4**, 20 (2016). https://doi.org/10.3389/fphy.2016.00020
240. L. Pentecoste, A.-L. Thomann, P. Brault, T. Lecas, P. Desgardin, T. Sauvage, M.-F. Barthe, Acta Mater. **141**, 47 (2017). https://doi.org/10.1016/j.actamat.2017.08.065
241. A. Delcorte, K. Moshkunov, M. Debongnie, J. Vac. Sci. Technol. B **36**, 03F109 (2018). https://doi.org/10.1116/1.5012981
242. A.A. Sycheva, E.N. Voronina, T.V. Rakhimova, J. Surf. Investig. **12**, 1270 (2018). https://doi.org/10.1134/S1027451019010191
243. J. Jussila, F. Granberg, K. Nordlund, Nucl. Mater. Energy **17**, 113–122 (2018). https://doi.org/10.1016/j.nme.2018.08.002
244. A.A. Sycheva, E.N. Voronina, T.V. Rakhimova, A.T. Rakhimov, Appl. Surf. Sci. **475**, 1021 (2019). https://doi.org/10.1016/j.apsusc.2019.01.078
245. T. Gergs, T. Mussenbrock, J.A. Trieschmann, J. Appl. Phys. **132**, 063302 (2022). https://doi.org/10.1063/5.0098040
246. N. Lümmen, T. Kraska, Nanotechnology **15**, 525 (2004). https://doi.org/10.1088/0957-4484/15/5/021
247. N. Lümmen, T. Kraska, Nanotechnology **16**, 2870 (2005). https://doi.org/10.1088/0957-4484/16/12/023
248. N. Lümmen, T. Kraska, Phys. Rev. B **71**, 205403 (2005). https://doi.org/10.1103/PhysRevB.71.205403
249. N. Lümmen, T. Kraska, Eur. Phys. J. D **41**, 247 (2007). https://doi.org/10.1140/epjd/e2006-00210-4
250. P. Brault, Front. Phys. **6**, 59 (2018). https://doi.org/10.3389/fphy.2018.00059
251. P. Brault, W. Chamorro-Coral, S. Chuon, A. Caillard, J.-M. Bauchire, S. Baranton, C. Coutanceau, E. Neyts, Front. Chem. Sci. Eng. **13**, 324 (2019). https://doi.org/10.1007/s11705-019-1792-5
252. E. Goudeli, Curr. Opin. Chem. Eng. **23**, 155 (2019). https://doi.org/10.1016/j.coche.2019.04.001
253. P. Grammatikopoulos, Curr. Opin. Chem. Eng. **23**, 164 (2019). https://doi.org/10.1016/j.coche.2019.04.004
254. J.-G. Mattei, P. Grammatikopoulos, J. Zhao, V. Singh, J. Vernieres, S. Steinhauer, A. Porkovich, E. Danielson, K. Nordlund, F. Djurabekova, M. Sowwan, Chem. Mater. **31**, 2151 (2019). https://doi.org/10.1021/acs.chemmater.9b00129
255. P. Brault, Energies **13**, 3584 (2020). https://doi.org/10.3390/en13143584
256. B.S.R. Kouamé, S. Baranton, P. Brault, C. Canaff, W. Chamorro-Coral, A. Caillard, K. De Oliveira Vigier, C. Coutanceau, Electrochimica Acta 329, 135161 (2020). https://doi.org/10.1016/j.electacta.2019.135161
257. K.-H. Müller, Surf. Sci. **184**, L375 (1987). https://doi.org/10.1016/S0039-6028(87)80265-0
258. K.H. Müller, J. Appl. Phys. **62**, 1796 (1987). https://doi.org/10.1063/1.339559
259. K.H. Müller, J Vac. Sci. Technol. A **6**, 1690 (1988). https://doi.org/10.1116/1.575309
260. I. Kwon, R. Biswas, G.S. Grest, C.M. Soukoulis, Phys. Rev. B **41**, 3678 (1990). https://doi.org/10.1103/PhysRevB.41.3678
261. C.M. Gilmore, J.A. Sprague, Phys. Rev. B **44**, 8950 (1991). https://doi.org/10.1103/PhysRevB.44.8950
262. C. C. Fang, F. Jones, V. Prasad, MRS Online Proceedings Library (OPL) , Volume 280. In: Symposium B—Evolution of Surface and Thin Film Microstructure, 463 (1992). https://doi.org/10.1557/PROC-280-463
263. C.C. Fang, V. Prasad, F. Jones, J. Vac. Sci. Technol. A **11**, 2778 (1993). https://doi.org/10.1116/1.578641
264. C.C. Fang, F. Jones, V. Prasad, J. Appl. Phys. **74**, 4472 (1993). https://doi.org/10.1063/1.354363
265. C.C. Fang, F. Jones, R.R. Kola, G.K. Celler, V. Prasad, J. Vac. Sci. Technol. B **11**, 2947 (1993). https://doi.org/10.1116/1.586566
266. R.W. Smith, F. Ying, D.J. Srolovitz, MRS Online Proc. Library **403**, 39 (1995). https://doi.org/10.1557/PROC-403-39
267. N.A. Marks, D.R. McKenzie, B.A. Pailthorpe, Phys. Rev. B **53**, 4117 (1996). https://doi.org/10.1103/PhysRevB.53.4117
268. F. Ying, R.W. Smith, D.J. Srolovitz, Appl. Phys. Lett. **69**, 3007 (1996). https://doi.org/10.1063/1.116821
269. J.D. Kress, D.E. Hanson, A.F. Voter, J. Vac. Sci. Technol. A **17**, 2819 (1999). https://doi.org/10.1116/1.581948
270. U. Hansen, S. Rodgers, K.F. Jensen, Phys. Rev. B **62**, 2869 (2000). https://doi.org/10.1103/PhysRevB.62.2869
271. S.-P. Ju, C.-I. Weng, J.-G. Chang, C.-C. Hwang, Surf. Coat. Technol. **149**, 135 (2002). https://doi.org/10.1016/S0257-8972(01)01445-1
272. S.-P. Ju, C.-I. Weng, J.-G. Chang, C.-C. Hwang, J. Vacuum Sci. Technol. B **20**, 946 (2002). https://doi.org/10.1116/1.1477423
273. C.-C. Hwang, J.G. Chang, S.P. Ju, J. Chin. Soc. Mech. Eng. Trans. Chin. Inst. Eng. Ser. C/Chung-Kuo Chi Hsueh Kung Ch'eng Hsuebo Pao **24**, 309 (2003)
274. X.W. Zhou, D.A. Murdick, B. Gillespie, H.N.G. Wadley, Phys. Rev. B **73**, 045337 (2006). https://doi.org/10.1103/PhysRevB.73.045337
275. K. Barmak, J. Kim, C.S. Kim, W.E. Archibald, G.S. Rohrer, A.D. Rollett, D. Kinderlehrer, S. Ta'asan, H. Zhang, D.J. Srolovitz, Scripta Mater. **54**, 1059 (2006). https://doi.org/10.1016/j.scriptamat.2005.11.060
276. T.B. Ma, Y.-Z. Hu, H. Wang, X. Li, Phys. Rev. B **75**, 035425 (2007). https://doi.org/10.1103/PhysRevB.75.035425
277. B.-H. Chen, C.-K. Chen, S.C. Chang, Nucl. Instrum. Methods Phys. Res. Sect. B **260**, 517 (2007). https://doi.org/10.1016/j.nimb.2007.03.105
278. D. Adamović, V. Chirita, E.P. Münger, L. Hultman, J.E. Greene, Phys. Rev. B **76**, 115418 (2007). https://doi.org/10.1103/PhysRevB.76.115418
279. Z.-H. Hong, S.-F. Hwang, T.-H. Fang, Comput. Mater. Sci. **41**, 70–77 (2007). https://doi.org/10.1016/j.commatsci.2007.03.004
280. V. Georgieva, M. Saraiva, N. Jehanathan, O.I. Lebelev, D. Depla, A. Bogaerts, J. Phys. D Appl. Phys. **42**, 065107 (2009). https://doi.org/10.1088/0022-3727/42/6/065107
281. N. Baguera, V. Georgieva, L. Calderin, I.T. Todorov, S. Van Gils, A. Bogaerts, J. Cryst. Growth **311**, 4034 (2009). https://doi.org/10.1016/j.jcrysgro.2009.06.034

282. V. Georgieva, I.T. Todorov, A. Bogaerts, Chem. Phys. Lett. **485**, 315 (2010). https://doi.org/10.1016/j.cplett.2009.12.067
283. Z.-H. Hong, S.-F. Hwang, T.-H. Fang, Comput. Mater. Sci. **48**, 520–528 (2010). https://doi.org/10.1016/j.commatsci.2010.02.018
284. A.-P. Prskalo, S. Schmauder, C. Ziebert, J. Ye, S. Ulrich, Comput. Mater. Sci. **50**, 1320 (2011). https://doi.org/10.1016/j.commatsci.2010.08.006
285. Z.H. Xu, L. Yuan, D.B. Shan, B. Guo, Comput. Mater. Sci. **50**, 1432 (2011). https://doi.org/10.1016/j.commatsci.2010.11.030
286. S.A. Roncancio, D.F. Arias-Mateus, M.M. Gómez-Hermida, J.C. Riaño-Rojas, E. Restrepo-Parra, Appl. Surf. Sci. **258**, 4473–4477 (2012). https://doi.org/10.1016/j.apsusc.2012.01.009
287. J. Houska, S. Mraz, J.M. Schneider, J. Appl. Phys. **112**, 073527 (2012). https://doi.org/10.1063/1.4757010
288. G. Kokkoris, P. Brault, A.-L. Thomann, A. Caillard, D. Samelor, A.G. Boudouvis, C. Vahlas, Thin Solid Films **536**, 115 (2013). https://doi.org/10.1016/j.tsf.2013.03.098
289. L. Xie, P. Brault, A.-L. Thomann, L. Bedra, Appl. Surf. Sci. **274**, 164 (2013). https://doi.org/10.1016/j.apsusc.2013.03.004
290. L. Xie, P. Brault, A.-L. Thomann, J.-M. Bauchire, Appl. Surf. Sci. **285**, 810 (2013). https://doi.org/10.1016/j.apsusc.2013.08.133
291. T. Zientarski, D. Chocyk, Thin Solid Films **562**, 347 (2014). https://doi.org/10.1016/j.tsf.2014.03.072
292. L. Xie, P. Brault, C. Coutanceau, A. Caillard, J. Berndt, E.C. Neyts, Appl. Catal. B **162**, 21 (2015). https://doi.org/10.1016/j.apcatb.2014.06.032
293. L. Xie, P. Brault, A.-L. Thomann, X. Yang, Y. Zhang, G.Y. Shang, Intermetallics **68**, 78 (2016). https://doi.org/10.1016/j.intermet.2015.09.008
294. S.S. Firouzabadi, K. Dehghani, M. Naderi, F. Mahboubi, Appl. Surf. Sci. **367**, 197 (2016). https://doi.org/10.1016/j.apsusc.2015.12.075
295. J.W. Abraham, T. Strunskus, F. Faupel, M. Bonitz, J. Appl. Phys. **119**, 185301 (2016). https://doi.org/10.1063/1.4948375
296. A.D. Pogrebnjak, O.V. Bondar, G. Abadias, V. Ivashchenko, O.V. Sobol, S. Jurga, E. Coy, Ceram. Int. **42**, 11743 (2016). https://doi.org/10.1016/j.ceramint.2016.04.095
297. M. Nikravesh, G.H. Akbari, A. Poladi, Tribol. Int. **105**, 185 (2017). https://doi.org/10.1016/j.triboint.2016.10.010
298. D. Edström, D.G. Sangiovanni, L. Hultman, I. Petrov, J.E. Greene, V. Chirita, J. Appl. Phys. **121**, 025302 (2017). https://doi.org/10.1063/1.4972963
299. G. Zhu, J. Sun, L. Zhang, Z. Gan, J. Cryst. Growth **492**, 60 (2018). https://doi.org/10.1016/j.jcrysgro.2018.04.002
300. X. Zhou, X. Yu, D. Jacobson, G.B. Thompson, Appl. Surf. Sci. **469**, 537 (2019). https://doi.org/10.1016/j.apsusc.2018.09.253
301. M. Kateb, H. Hajihoseini, J.T. Gudmundsson, S. Ingvarsson, J. Vacuum Sci. Technol. A **37**, 031306 (2019). https://doi.org/10.1116/1.5094429
302. M. Kateb, J.T. Gudmundsson, S. Ingvarsson, J. Vacuum Sci. Technol. A **38**, 043006 (2020). https://doi.org/10.1116/6.0000233
303. A.V. Pham, T.H. Fang, A.S. Tran, T.H. Chen, J. Phys. Chem. Solids **147**, 109663 (2020). https://doi.org/10.1016/j.jpcs.2020.109663
304. M. Zhang, Z. Rao, K.S. Kim, Y. Qi, L. Fang, K. Sun, E. Chason, Materialia **16**, 101043 (2021). https://doi.org/10.1016/j.mtla.2021.101043
305. M. Kateb, J.T. Gudmundsson, P. Brault, A. Manolescu, S. Ingvarsson, Surf. Coat. Technol. **426**, 127726 (2021). https://doi.org/10.1016/j.surfcoat.2021.127726
306. A.P. Thompson, H.M. Aktulga, R. Berger, D.S. Bolintineanu, W.M. Brown, P.S. Crozier, P.J. I'nt Veld, A. Kohlmeyer, S.G. Moore, T.D. Nguyen, R. Shan, M.J. Stevens, J. Tranchida, C. Trott, S.J. Plimpton, Comput. Phys. Commun. **271**, 10817 (2022). https://doi.org/10.1016/j.cpc.2021.108171
307. URL: https://www.lammps.org/
308. R. Li, L. Xie, W.Y. Wang, P.K. Liaw, Y. Zhang, Front. Mater. **7**, 290 (2020). https://doi.org/10.3389/fmats.2020.00290
309. A. Deschamps, F. Tancret, I.-E. Benrabah, F. De Geuser, H.P. Van Landeghem, C. R. Phys. **19**, 737 (2018). https://doi.org/10.1016/j.crhy.2018.08.001

Springer Nature or its licensor (e.g. a society or other partner) holds exclusive rights to this article under a publishing agreement with the author(s) or other rightsholder(s); author self-archiving of the accepted manuscript version of this article is solely governed by the terms of such publishing agreement and applicable law.

Pascal Brault is a Senior Scientist with CNRS at GREMI UMR7344 University of Orleans, France. He received his PhD in 1988 on Theoretical Atomic and Molecular Physics. His work deals with experiments, molecular dynamics simulations, and technology transfer of plasma-designed materials for energy, and recently with plasma wastewater treatments. He is co-author of more than 150 publications in international peer review journals. He is member of European Physical Society since 1991. He was granted Alexander von Humboldt Fellow in 1992–1993 by the Max Planck Institute für Strömungsforschung, Göttingen, Germany, headed by Professor Jan-Peter Toennies.

Anne-Lise Thomann is a senior scientist working on the deposition of functional oxides and multi-element metallic alloys by (reactive or not) magnetron sputter deposition. She obtained her PhD in 1995. She was hired in the GREMI laboratory in 1996. She focused her research on the mechanisms of metallic thin-film growth by magnetron sputter deposition. The GREMI's magnetron sputtering team, she used to coordinate, is now internationally recognized. Her scientific approach is to combine plasma/gas phase analysis, energy transfer measurements, and material characterization in order to both, understand the elementary processes involved (in the sputtering process at the target and in the film growth at the substrate) and control the final properties of the films. She is the head of the GREMI laboratory since January 2018.

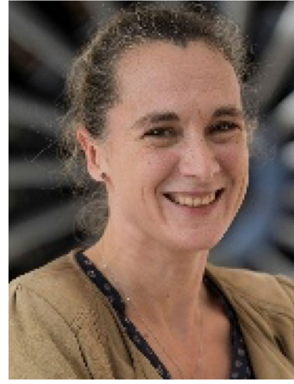

Marjorie Cavarroc is a senior R&T engineer in Safran. She is an expert in dry surface treatments. She has a long experience in the correlation between process parameters, textures, microstructures and properties of functional materials. Her current interests range from the search for innovative multifunctional materials to the development of green processes to elaborate nanostructured materials, for applications in energy, aerospace and aeronautical industries. She has co-authored 23 peer-reviewed articles, 64 oral presentations, 8 invited conferences, and 12 patents.